Hypothesis testing variables applied to trajectory fitting in the BaBar experiment

by

Paul D. Jackson

A Thesis Submitted in Partial Fulfillment of the
Requirements for the Degree of

MASTER OF SCIENCE

in the Department of Physics and Astronomy.

We accept this thesis as conforming
to the required standard.

Dr. R. V. Kowalewski, Supervisor (Department of Physics and Astronomy)

Dr. M. Lefebvre, Departmental Member (Department of Physics and Astronomy)

Dr. J. M. Roney, Departmental Member (Department of Physics and Astronomy)

Dr. S. E. Dosso, Outside member (Department of Earth and Ocean Science)

Dr. C. Hearty, External examiner (Department of Physics and Astronomy, UBC)

Supervisor: Dr. R. V. Kowalewski

Abstract

The ability to find deviations that arise between the trajectory assumed in a fit to a set of measurements and the actual trajectory, has been examined using a set of hypothesis testing variables. These variables are applied to information from the tracking volume of the BaBar detector at PEP-II. The extent to which improvements can be made in the rejection of single tracks that contain a discrete deviation (such as $\pi \rightarrow \mu$ decay-in-flight) has been studied. Using Monte Carlo techniques, different trajectory errors were considered and these hypothesis testing variables were utilised in an attempt to discriminate between well fitted and poorly fitted trajectories. The hypothesis tests were also performed on real data.

Examiners:

Dr. R. V. Kowalewski, Supervisor (Department of Physics and Astronomy)

Dr. M. Lefebvre, Departmental Member (Department of Physics and Astronomy)

Dr. J. M. Roney, Departmental Member (Department of Physics and Astronomy)

Dr. S. E. Dosso, Outside member (Department of Earth and Ocean Science)

Dr. C. Hearty, External examiner (Department of Physics and Astronomy, UBC)

Contents

List of Tables

List of Figures

Acknowledgements

My thanks go to my supervisor, Bob Kowalewski. His guidance, words of wisdom and patience have been crucial to this analysis. Were it not for his comments and his understanding these acknowledgements may well not have a thesis to accompany them. I would also like to thank the other members of the University of Victoria Particle Physics group for maintaining a healthy and relaxed working environment.

I want to praise some friends that keep me sane. Dom, Eric and all the other graduate students out here in Victoria. Paul (Brother P), Bobby Edwards (coolest man in England), Tom, Simon, Chris, Bill, Chris Sheehan (you magnificent bastard !), Marie and the girls, the Furness boys and everyone else whose name may not be down here but knows who they are. Cheers !

Last, but by no means least, my mum and dad. Without you I am literally nothing, I'm eternally grateful for everything you do for me. I love you both.

Chapter 1

Introduction

The discipline of particle physics wishes to answer questions regarding the ultimate reality of the physical Universe. One puzzle is the observed matter/anti-matter asymmetry of the Universe and the BaBar experiment has been constructed to test one theory that may go some way to explaining it. The research described here is designed to impact the tracking reconstruction of the BaBar experiment. We will develop and evaluate methods to improve the rejection of badly reconstructed tracks, namely those where a trajectory that has been reconstructed from a set of hits as a single track actually contained a deviation that was not recognised. Such deviations are commonly referred to as kinks. One process by which a reconstructed trajectory may contain a kink is the decay-in-flight of a charged pion to a muon and an associated neutrino. This decay may go undetected, in which case, an unkinked track would be fitted to a set of hits that contain a kink. Failure to detect the kink in this case would result in background in the prompt muon sample.

The experimental goal of BaBar is the measurement of CP asymmetries in the B meson system. The theory behind this section of the Standard Model and the context in which it is pertinent to the work presented here, will be discussed in more detail in chapter 2. Having

been designed with specific measurements in mind, there were many criteria that the BaBar detector had to meet to enable the determination of CP asymmetries. The detector will be described in chapter 3 with an explanation given of how each subdetector is tuned to meet specific physics goals.

Measuring CP asymmetries requires the B flavour to be tagged. Muon identification in BaBar is relevant in the use, for instance, of prompt muons from semi-leptonic B decays to determine the flavour of the parent B particle. This in turn is used to tag the flavour of the other B in the event. Therefore, identification of the decay-in-flight of a charged pion to a muon will enable the reduction of fake muon signals in the outer chambers of the detector. Since these fake signals may mimic a prompt muon signal, which may in turn be used to tag B flavour, reducing them assists in the reduction of mis-tagging. Further discussion of this will be left until chapter 2.

The decay-in-flight of a charged pion to a muon is not the only process by which a deviation in a single fitted trajectory may arise. A discrete change at some point may arise from a scattering for example, while a continuous parameter change may arise from dE/dx energy loss or magnetic field anomalies. Such deviations introduce correlated shifts in the positions of sequential measurements. To assist in finding badly reconstructed tracks we will introduce novel test statistics, which can be calculated for fitted tracks in real data. These statistics will be applied to address the goodness-of-fit of each individual track and compared to the usual $P(\chi^2)$ test. They are presented in chapter 4. These tests may be applied to the output of a Kalman filter, a method of sequential fitting used in BaBar which can account for known sources of correlation. The aim here is to seek statistics that allow us

to discriminate between tracks with and without deviations. Specific Monte Carlo samples of single muons and single pions (with the pion lifetime reduced by a factor of 100 for increased probability of decays) were generated to investigate the extent to which these statistics could remove $\pi^+ \rightarrow \mu^+\nu_\mu$(+ charge conjugate) decays. For a fixed fraction of muons surviving a specific cut on a test statistic (or hypothesis testing variable as they will be called in later sections) the number of pion decay events surviving is examined. The rejection achieved in this sample was then compared to a sample of simulated $B\bar{B}$ events from the BaBar Monte Carlo. Other methods by which kinks may arise were also examined and furthermore, the extent to which these variables perform on the real data of BaBar is studied. These results are presented in chapter 5.

Chapter 2

Theory

2.1 The Standard Model, Quark Mixing and the CKM matrix

The Standard Model describes the interactions of elementary particles under the influence of the strong, weak and electromagnetic forces. These are three of the four fundamental forces of nature; the gravitational force is the weakest and has no measurable effect on the subatomic scale. The theory of Quantum Chromodynamics describes the strong interaction while the weak and electromagnetic interactions are described by the unified electroweak theory [1–3]. The strong force is mediated by gluons which are responsible for binding quarks together into hadrons. The weak force occurs by exchanging one of three intermediate vector bosons (the $W^{\pm}$ and Z^0) and the electromagnetic force is characterised by the emission or exchange of a photon which couples to the electric charge of the interacting particle.

The elementary particles can be categorised as quarks and leptons, each of which are divided into three generations. Experimental evidence exists for all six quarks and leptons. As we will describe below, W-boson-mediated interactions between quarks of different generations are allowed and described by the CKM matrix [4]. This is in contrast to leptons,

where interactions between generations do not occur in the Standard Model. Table 2.1 gives an outline of the properties of the fermions, where we split the table into three generations horizontally. Each particle has an associated antiparticle, with an opposite electric charge. The reason for the absolute mass scale or the progression towards higher masses between generations is not known.

Leptons			Quarks		
Flavour	Charge	Mass(GeV)	Flavour	Charge	Mass
ν_e	0	$< 3 \times 10^{-9}$	u	$+\frac{2}{3}$	1 - 5 MeV
e	-1	5.11×10^{-4}	d	$-\frac{1}{3}$	3 - 9 MeV
ν_μ	0	$< 1.9 \times 10^{-4}$	c	$+\frac{2}{3}$	1.15 - 1.35 GeV
μ	-1	0.106	s	$-\frac{1}{3}$	75 - 170 MeV
ν_τ	0	$< 18 \times 10^{-3}$	t	$+\frac{2}{3}$	174.3 ± 3.1 GeV
τ	-1	1.78	b	$-\frac{1}{3}$	4.0 - 4.4 GeV

Table 2.1: Some properties of the fundamental constituents of matter in the Standard Model. Electric charge is given in units of positron charge. The masses given are the Particle Data Book 2000 evaluations [5].

Those quarks and leptons that have an electric charge undergo electromagnetic interactions, which are mediated by the photon. Quark flavour is conserved in these interactions. All quarks and leptons interact via the charged and neutral weak currents, which are mediated by the $W^{\pm}$ and Z^0 bosons, respectively. As is the case for the electromagnetic interaction, weak neutral-current interactions conserve quark flavour. In charged-current interactions on the other hand, processes such as $b \rightarrow W^{*-}u$ are allowed, provided that the quarks are left-handed (the notation W^{*-} is used to denote a virtual W^-). In addition, $W^- \rightarrow l^-\bar{\nu}_l$ decays are allowed, and governed by a universal coupling constant, g, which is commonly written in terms of $\sin^2\theta_W$. θ_W is the Weinberg weak mixing angle between the electromagnetic and weak interactions, and $\sin^2\theta_W$ is expressible as a function of the electromagnetic charge e,

and g thus,

$$e = g \sin\theta_W . \tag{2.1}$$

The Cabibbo-Kobayashi-Maskawa (CKM) matrix, V_{CKM}, describes the relative size of the charged-current weak amplitudes between quarks. For the reaction $q \rightarrow W^{*-}Q$, where q is a -1/3 charged quark and Q has a charge of +2/3, the coupling is gV_{Qq}, where V_{Qq} can in general be complex. For the reaction $Q \rightarrow W^{*+}q$, the coupling is gV^*_{Qq}. With three generations, V_{CKM} is a 3 x 3 matrix :

$$V_{CKM} = \begin{pmatrix} V_{ud} & V_{us} & V_{ub} \\ V_{cd} & V_{cs} & V_{cb} \\ V_{td} & V_{ts} & V_{tb} \end{pmatrix} . \tag{2.2}$$

V_{CKM} provides a connection between quark mass eigenstates (q = (d, s, b)) and weak current eigenstates (q′ = (d′, s′, b′)), so that $q' = V_{CKM}q$. In this way, V_{CKM} as written here is unitary, assuming that there exists exactly three generations of quarks. Additional generations would be denoted as extra columns and rows in the matrix.

2.2 The Unitarity Triangle

The properties of the CKM matrix may be shown in a number of different parameterizations. The Wolfenstein parameterization [5,6] is a popular approximation where one fixes λ as the sine of the well-measured Cabibbo angle [7] and then writes the other elements in terms of powers of λ

$$V \approx \begin{pmatrix} 1-\lambda^2/2 & \lambda & A\lambda^3(\rho - i\eta) \\ -\lambda & 1-\lambda^2/2 & A\lambda^2 \\ A\lambda^3(1-\rho-i\eta) & -A\lambda^2 & 1 \end{pmatrix} + \vartheta(\lambda^4). \tag{2.3}$$

Tests of unitarity in a CKM matrix consisting of three generations provide ways to search

for new physics. Of particular interest is the orthogonality of the first and third columns,

$$V_{ud}V_{ub}^{*} + V_{cd}V_{cb}^{*} + V_{td}V_{tb}^{*} = 0. \tag{2.4}$$

Thus,

$$\frac{-V_{ud}V_{ub}^{*}}{V_{cd}V_{cb}^{*}} + \frac{-V_{td}V_{tb}^{*}}{V_{cd}V_{cb}^{*}} = 1. \tag{2.5}$$

Additionally if we choose both V_{cd} and V_{cb} to be real[1], then,

$$\frac{-V_{ud}V_{ub}^{*}}{|V_{cd}V_{cb}|} + \frac{-V_{td}V_{tb}^{*}}{|V_{cd}V_{cb}|} = 1. \tag{2.6}$$

This constraint is illustrated in figure 2.1 and is commonly referred to as the "unitarity triangle". It is important to note that the lengths of all three sides as written above are proportional to λ^0. The existing experimentally measured constraints on the apex of the unitarity triangle are shown in figure 2.2. The fitting procedure for this plot is described in the "Overall determinations of the CKM matrix" in [9].

2.3 Why study B physics?

There are several reasons why B physics is an interesting area in which to probe the Standard Model and in particular the CKM matrix of quark-mixing and CP violation. The CP violating phase of the three generation CKM matrix provides an elegant explanation of the well-established CP violating effects seen in K_L^0 decays. However, studies of CP violation in neutral kaon decays and the resulting experimental constraints on the parameters of the CKM matrix do not in fact provide a test of whether the CKM phase describes CP violation.

[1] We are free to choose this parameterization since we can always choose to orient the triangle as we see fit.

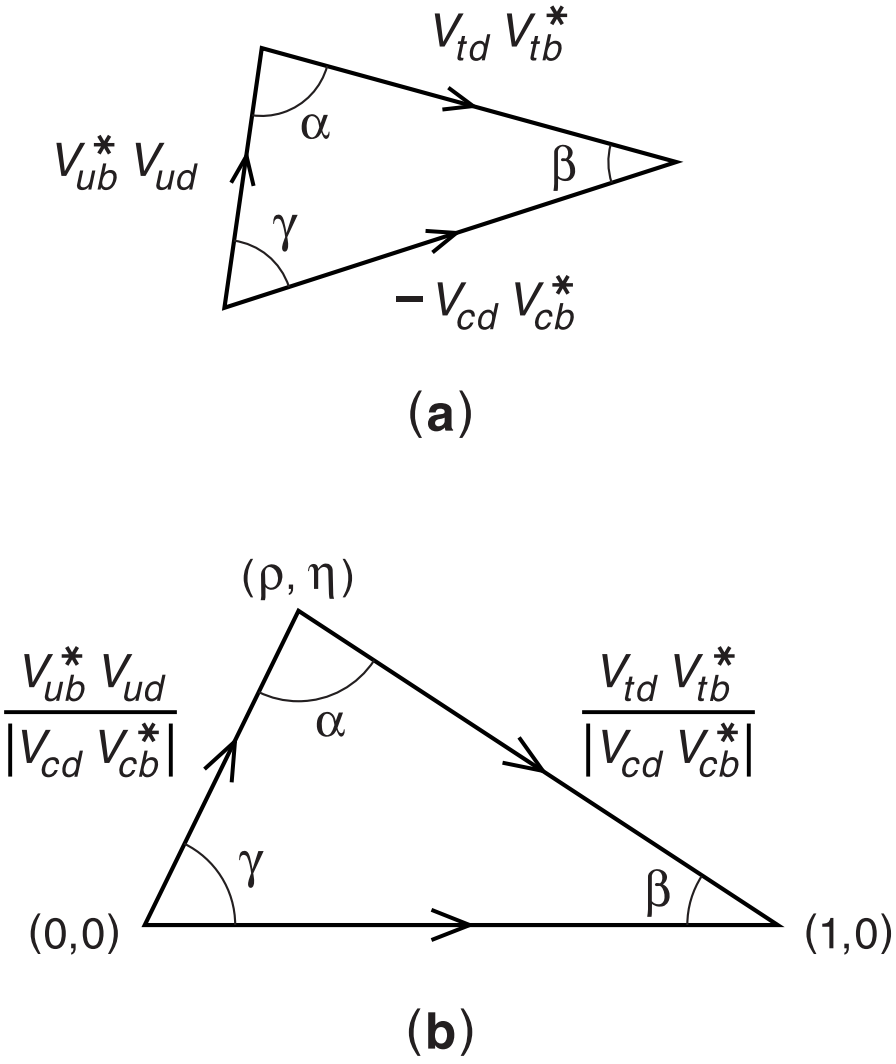

Figure 2.1: The CKM unitarity triangle based on the orthogonality between the first and third columns of the CKM matrix [8]

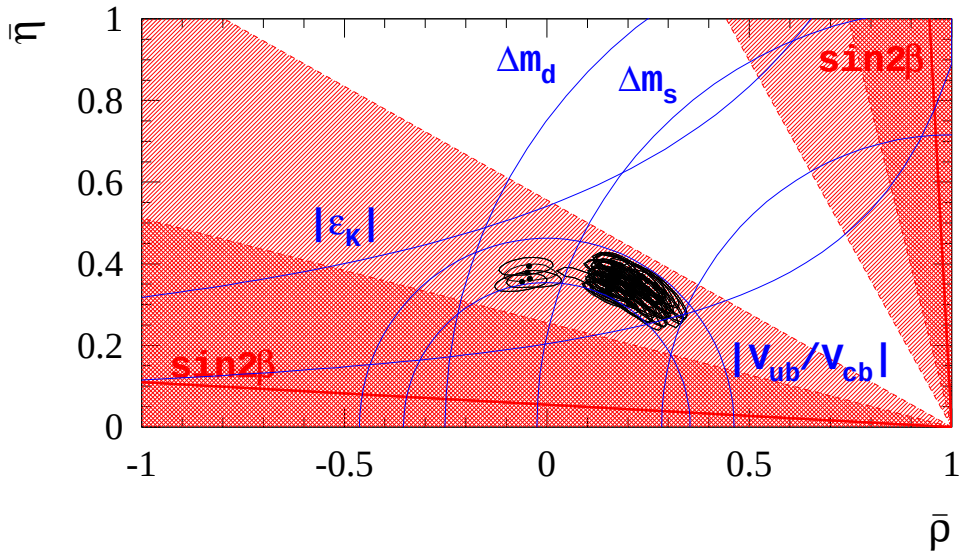

Figure 2.2: Present constraints on the position of the apex of the unitarity triangle in the $(\overline{\rho}, \overline{\eta})$ plane. Each contour centred with a dot represents the 95% confidence level for a fixed set of theoretical parameters. Δm_s arises from B_s mixing and is a single line which excludes the region to the left. Δm_d is found experimentally from B_d mixing and has upper and lower bounds. Each of these curves corresponds to a circle centred at $\overline{\rho} = 1$. Constraints from $|\epsilon_k|$ measurements are shown bound by two hyperbolas. $|\frac{V_{ub}}{V_{cb}}|$ constrains the apex within the semi-circular bands enclosed by the $\overline{\rho}$ axis. There is two-fold ambiguity in deriving a value of β from a measurement of sin2β. These choices are shown in the cross-hatched regions, which correspond to the 1σ and 2σ bands around the central value for $\sin 2\beta$ measured by the BaBar collaboration.

If we examine the CKM matrix as written in equation 2.3 one can see that there are four parameters (λ, A, ρ and η) that are contained in the nine elements. The parameters A, ρ and η are only accessible through looking at reactions involving third generation quarks.

This provides a direct reason to look at the physics of the b quark. At present energies it is the only third generation quark that is readily accessible in large numbers. This sensitivity allows measurements to be made in order to determine many of the properties of the unitarity triangle, as shown in figure 2.1. The angle β can be obtained in BaBar using, for example, the decay $B^0 \rightarrow J/\psi\ K^0_S$ which will be mentioned in section 2.4.5. The angle α can be determined by the decay $B^0 \rightarrow \pi^{\pm}\pi^{\mp}$. Also information regarding the length of the side of the triangle (see figure 2.1) can be obtained by measuring $|V_{ub}|$ from, for instance, semi-leptonic B decays and $|V_{td}|$ via B^0_d oscillations. It is clear, therefore, that the B system provides a rich area in which to measure Standard Model parameters and also to search for non-Standard Model processes.

2.4 CP Violation in the B Meson System

As has been mentioned, the main aim of the BaBar experiment is to study CP violation in the neutral B meson system. CP violation is one of the least well tested aspects of the Standard Model and so far has been seen only in the neutral K meson system [10]. However, it is one of the necessary conditions to explain the baryon asymmetry of the universe [11] and is an essential property of the CKM picture of the quark sector [4]. In this we refer to the single Kobayashi-Maskawa phase in the CKM matrix which is the single source of CP violation in the Standard Model.

2.4.1 Neutral Meson Mixing

Consider a system of two degenerate states $|\psi_1\rangle$ and $|\psi_2\rangle$. Suppose an interaction exists to transform $|\psi_1\rangle$ into $|\psi_2\rangle$ and vice versa. If one starts off with an initially pure state of ψ_1 then at some time later one will in general have a $\psi_1 - \psi_2$ mixture and the eigenstates of the system will no longer be degenerate. If we consider only cases where the $|\psi_1\rangle$ and $|\psi_2\rangle$ are, in fact, particle and antiparticle, $|\psi\rangle$ and $|\overline{\psi}\rangle$, then, if A and B are the matrix elements of the possible mixing (which contain elements of the mass and decay matrices), we obtain for the time dependent parts of the Schrödinger equation

$$i\frac{\partial}{\partial t}\begin{pmatrix} |\psi\rangle \\ |\bar{\psi}\rangle \end{pmatrix} = \begin{pmatrix} A & B \\ B & A \end{pmatrix}\begin{pmatrix} |\psi\rangle \\ |\bar{\psi}\rangle \end{pmatrix}. \tag{2.7}$$

The eigenvalues are readily found to be $A+B$ and $A-B$ and the two decoupled modes are:

$$|\psi_+\rangle = \frac{1}{\sqrt{2}}(|\psi\rangle + |\overline{\psi}\rangle), \quad |\psi_-\rangle = \frac{1}{\sqrt{2}}(|\psi\rangle - |\overline{\psi}\rangle). \tag{2.8}$$

The original states $|\psi\rangle$ and $|\overline{\psi}\rangle$ are eigenstates of the strong interaction. These decoupled states, however, are eigenstates of mass and of CP. In particular,

$$\widehat{CP}|\psi_\pm\rangle = \pm|\psi_\pm\rangle. \tag{2.9}$$

Thus far the framework for a mixing, CP conserving neutral meson system has been outlined. To get the full picture, one must allow for the possibility of CP violation and rewrite the mixing equations thus

$$i\frac{\partial}{\partial t}\begin{pmatrix} |\psi\rangle \\ |\bar{\psi}\rangle \end{pmatrix} = \begin{pmatrix} A & B(p/q) \\ (q/p)B & A \end{pmatrix}\begin{pmatrix} |\psi\rangle \\ |\bar{\psi}\rangle \end{pmatrix}. \tag{2.10}$$

Again one can decouple the modes by diagonalising the matrix, the decoupled states are then found to be

$$|\psi_{\rm S}\rangle = q|\psi\rangle + p|\overline{\psi}\rangle, \quad |\psi_{\rm L}\rangle = q|\psi\rangle - p|\overline{\psi}\rangle \tag{2.11}$$

with the masses and widths of the states coming from the real and imaginery parts of $A \pm B$ as before. The fact that CP-violating effects are small means that q/p is approximately 1 and that $\psi_{\rm S}$ and $\psi_{\rm L}$ are almost the same as ψ_+ and ψ_-. In practice, it is convenient to use the parameter ϵ which is defined as

$$\epsilon = \frac{1 - q/p}{1 + q/p}. \tag{2.12}$$

2.4.2 Time Evolution of Neutral B_d Mesons

We define the light B_L and heavy B_H neutral $\mathrm{B_d}$ meson mass eigenstates as linear combinations of the flavour eigenstates

$$|\mathrm{B}_L\rangle = p|\mathrm{B}^0\rangle + q|\bar{\mathrm{B}}^0\rangle \tag{2.13}$$

$$|B_H\rangle = p|\mathrm{B}^0\rangle - q|\bar{\mathrm{B}}^0\rangle \tag{2.14}$$

where p and q are complex and obey the normalisation condition

$$|q|^2 + |p|^2 = 1. \tag{2.15}$$

The mass difference $\Delta m_{\rm B}$ and the width difference $\Delta ?_{\rm B}$ between the two states are defined as follows:

$$\Delta m_{\rm B} \equiv M_H - M_L, \quad \Delta ?_{\rm B} \equiv ?_H - ?_L, \tag{2.16}$$

so that $\Delta m_{\rm B}$ is positive by definition. The lifetime difference has not yet been measured but is expected to be negligible.

Any B state can be written as an admixture of B_H and B_L, with amplitudes that evolve in time

$$a_H(t) = a_H(0)e^{-iM_H t}e^{-\frac{1}{2}\Gamma_H t}, \quad a_L(t) = a_L(0)e^{-iM_L t}e^{-\frac{1}{2}\Gamma_L t}. \tag{2.17}$$

A state which is created at time $t = 0$ as a pure B^0 state has $a_L(0) = a_H(0) = 1/(2p)$. An initially pure $\bar{B}^0$ state has $a_L(0) = -a_H(0) = 1/(2q)$ (from equations 2.13 and 2.14). Taking the approximation $?_H = ?_L (= ?)$ gives the time evolution of these states to be

$$|B^0(t)\rangle = g_+(t)|B^0\rangle + (q/p)g_-(t)|\bar{B}^0\rangle, \tag{2.18}$$

$$|\bar{B}^0(t)\rangle = (p/q)g_-(t)|B^0\rangle + g_+(t)|\bar{B}^0\rangle, \tag{2.19}$$

where

$$g_+(t) = e^{-iMt}e^{-\frac{1}{2}\Gamma t}\cos(\Delta m_B t/2), \tag{2.20}$$

$$g_-(t) = e^{-iMt}e^{-\frac{1}{2}\Gamma t} i \sin(\Delta m_B t/2), \tag{2.21}$$

and $M = \frac{1}{2}(M_H + M_L)$. These results will be useful when we describe how CP violation arises in B decays.

2.4.3 Coherent Production of B Meson Pairs

This section considers the consequences of producing neutral B mesons at a 'B Factory', (such as BaBar) that is an e^+e^- collider operating at the $\Upsilon(4S)$ resonance. In this situation, the B^0 and $\bar{B}^0$ are produced in a *coherent state* with L=1. One way to view this state is that each of the two particles evolve in time as a single B would. However they evolve in phase such that at any one time, until one of them decays, they are always orthogonal linear combinations of B_L and B_H. After the decay of one of the particles, the other continues to evolve until it, in turn, decays.

Therefore one may exploit the flavour correlation between the two B's to determine the flavour of each B meson. To measure CP asymmetries one typically looks for events where one of the B mesons decays to a CP eigenstate final state $f_{\rm CP}$ at time t_f, while the second decays to a tagging mode, that is a mode which identifies its b-flavour, at a time t_{tag}. Say that one B was identified as a $\bar{B}^0$ through its decay to a tagging mode. This then identifies the *other* particle as a B^0 at time $t = t_{tag}$.

2.4.4 The Three types of CP Violation in B Decays

Given this knowledge of the time evolution, and mixing of neutral B mesons we can discuss the different ways in which CP violation can occur in this system. Study of both neutral and charged sectors has relevance to CP measurements. There are three possible manifestations of CP violation within the B meson system and these can be expressed in a model independent way :

1. CP violation in decay, which occurs in both charged and neutral decays, when the amplitude for a decay and its CP conjugate process have different magnitudes. This requires the contribution of at least two decay amplitudes.

2. CP violation in mixing, which results from the two neutral mass eigenstates being different from the CP eigenstates. Therefore $q/p \neq 1$ gives CP violation of this type.

3. CP violation in the interference between decays with and without mixing, which occurs in decays into final states that are common to B^0 and $\bar{B}^0$. It may occur in combination with the other two types but in BaBar there are cases when, to an excellent approximation, it is the only effect.

It is useful to identify a particular CP-violating quantity, for each case, that is independent of phase conventions, and discuss the types of processes that depend on this quantity. Since the third of the types mentioned is of specific relevance in BaBar this will be described in further detail in the following subsection. Much of what is to follow and information on the other two types of CP violation can be found in [9].

2.4.5 CP Violation in the Interference between Mixing and Decay

Now consider neutral B decays to final states which are eigenstates of CP, $f_{\rm CP}$. Such states are accessible in both $\rm B^0$ and $\rm \bar{B}^0$ decays. The physically meaningful phase convention independent quantity here is:

$$\lambda \equiv \frac{q}{p}\,\frac{\bar{A}_{f_{\rm CP}}}{A_{f_{\rm CP}}} = \eta_{f_{\rm CP}}\frac{q}{p}\,\frac{\bar{A}_{\bar{f}_{\rm CP}}}{A_{f_{\rm CP}}} \tag{2.22}$$

where $\eta_{f_{\rm CP}}(=\pm 1)$ is the CP eigenvalue of the state $f_{\rm CP}$ and

$$\bar{A}_{f_{\rm CP}} = \eta_{f_{\rm CP}}\bar{A}_{\bar{f}_{\rm CP}}. \tag{2.23}$$

When CP is conserved, $|q/p| = 1$, $|\bar{A}_{\bar{f}_{\rm CP}}/A_{f_{\rm CP}}| = 1$ and importantly for this type of CP violation, λ (not to be confused with the Wolfenstein λ) has no overall phase. In the absence of CP violation in decay and in the mixing ($|\lambda| = 1$) the time dependent CP asymmetry can be expressed as:

$$a_{f_{\rm CP}}(t) = -{\rm Im}(\lambda)\sin(\Delta m_{\rm B}{\rm t}) \tag{2.24}$$

where t is the time difference between the decays of the two B mesons, $\rm t_{f_{CP}} - t_{\mathit{tag}}$. Thus, even if CP violation in decay and CP violation in mixing are not present there can still be an asymmetry when ${\rm Im}(\lambda) \neq 0$. This is called CP *violation in the interference between decays*

with and without mixing here. It is sometimes abbreviated to, "interference between mixing and decay".

An example of a decay through which the angle β of the unitarity triangle can be measured is $B^0 \to J/\psi\ K^0_S$. Recall that we defined λ previously in equation 2.22. The q/p part of this comes from B^0 mixing processes such as those in figure 2.3(a). There is also an extra contribution to λ to account for K^0 mixing:

$$\lambda = \left(\frac{q}{p} \right) \left(\frac{\bar{A}}{A} \right) \left(\frac{q}{p} \right)_K \tag{2.25}$$

The decay part is given by tree level processes such as those in figure 2.3(b):

$$\frac{\bar{A}}{A} = \frac{V_{cb} V^*_{cs}}{V^*_{cb} V_{cs}} \tag{2.26}$$

and the full expression is

$$\lambda(B^0 \to J/\psi\ K^0_S) = \left(\frac{V^*_{tb} V_{td}}{V_{tb} V^*_{td}} \right) \left(\frac{V_{cb} V^*_{cs}}{V^*_{cb} V_{cs}} \right) \left(\frac{V_{cs} V^*_{cd}}{V^*_{cs} V_{cd}} \right) \tag{2.27}$$

which gives

$$\mathrm{Im}(\lambda) = -\sin(2\beta). \tag{2.28}$$

This quantity can be measured as is shown in equation 2.24.

2.5 The physics impact of this research

The specific importance of the $B^0 \to J/\psi\ K^0_S$ decay mode mentioned in section 2.4.5 to the work presented here lies in the reconstruction of the B meson, and more specifically the tagging of B meson flavour. Muon identification is used in tagging the flavour of the

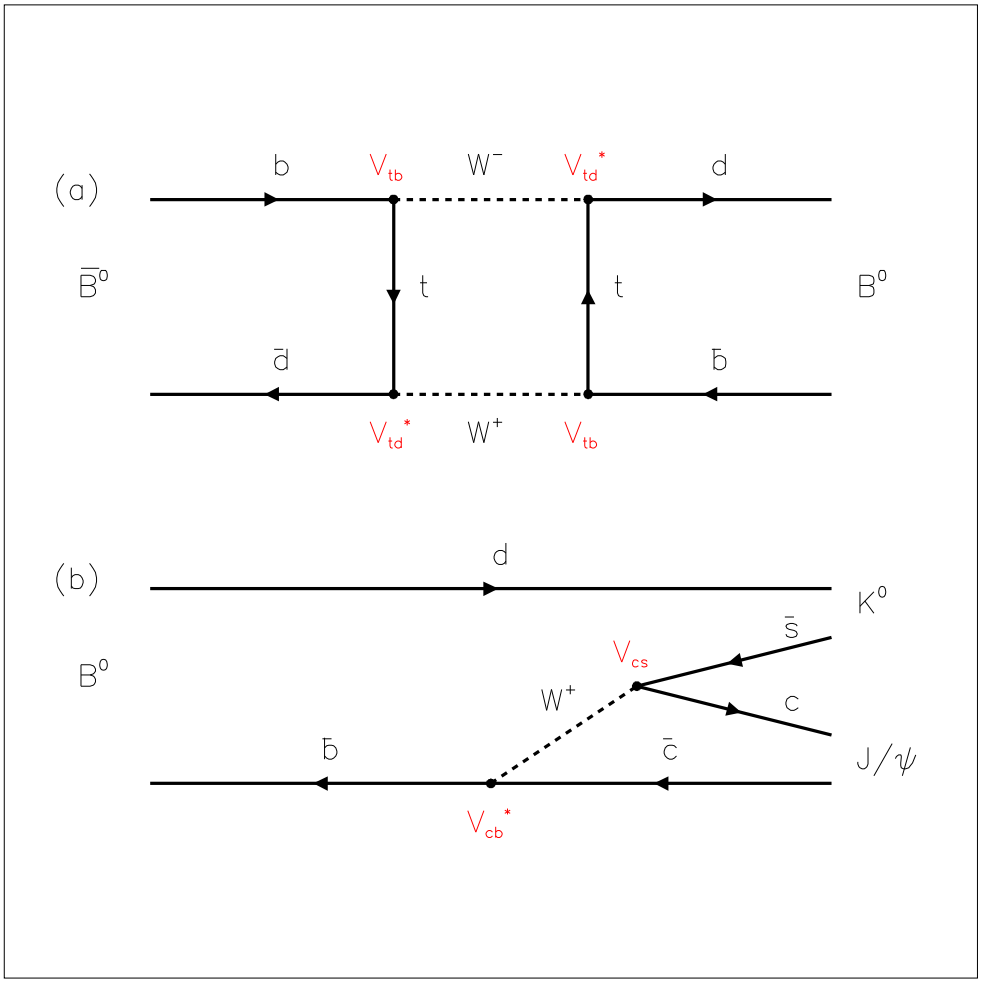

Figure 2.3: Feynmann diagrams for (a) neutral B meson mixing and (b) a typical tree level diagram.

parent B particle through semi-leptonic decays such as B $\rightarrow$ X $\mu\nu$, where the X represents a meson, and the muon charge indicates the charge of the weakly decaying b quark[2]. For this kind of measurement to be successful and accurate, good muon identification is vital and so any contamination in the muon chambers from fake signals arising from decays, such as $\pi^+ \rightarrow \mu^+\nu_\mu$(+ charge conjugate) for example, may degrade the ability to determine the b flavour.

For events where one B has been reconstructed in a CP eigenstate, decay products from the other B are used to determine the tagging category. The measured asymmetry is associated to the true asymmetry by a dilution factor(D). We can write this as $a_{obs}(t) = D \cdot a_{true}(t)$, where a_{obs} and a_{true} are the measured and the true asymmetries respectively. For each tagging category (muons for example) the dilution factor is given by $D_i = (1 - 2w_i)$, where w_i is the mis-tag fraction, the probability of wrongly assigning the opposite tag to an event of this category.

However, this study will not only be interested in decays-in-flight. We will be seeking methods by which tracks which may have some error in their reconstruction can be identified and dealt with accordingly. This is important since cleaning up tracking samples and identifying processes by which bad tracks arise enables us to correct mistakes, reduce measurement errors on calculations and work with tracks of greater accuracy.

[2]A caveat to this is a lepton originating from a cascade decay (b $\rightarrow$ c $\rightarrow$ s) in which case the sign of the charge may be opposite that of the b quark. One can distinguish between leptons from cascades and leptons from semi-leptonic decays by using the momentum of the lepton in the Υ(4S) rest frame.

Chapter 3

The BaBar Detector

3.1 Introduction

In order to measure CP asymmetries in many different B meson decay modes the BaBar detector had to meet certain criteria. In general there should be the maximum possible acceptance in the center-of-mass system. In order to measure CP asymmetries successfully one needs to accurately measure Δt, the difference in the decay times of the two B mesons. The SLAC B factory employs an asymmetric collider, where the beams of electrons and positrons are of differing energies, and occupy separate rings. The detector is necessarily asymmetric to account for this effect as well as possible. To provide enough B mesons to measure rare decay modes, the machine must operate at high luminosity[1]. The high luminosity of PEP-II requires that some machine components be very close to the interaction region (see later) and these had to be accomodated in the detector design. The detector also requires excellent momentum resolution for charged particles, excellent energy resolution for

[1]Where luminosity is the number of particles per unit time per unit area or the reaction rate divided by the interaction cross-section

photons and excellent mass resolution for all particle types. Another requirement here is the need to minimize multiple scattering. It should be possible to track charged particles over the range $\sim$60 MeV/c $< P_t <$ $\sim$4 GeV/c. Good lepton and kaon identification is necessary for fully reconstructing B decays and distinguishing amongst final states.

More specifically, individual sections of the detector have their own requirements geared towards achieving the best possible physics performance. The vertex resolution must be excellent since the difference in decay time of the two B mesons is measured in terms of the difference in the z-components (where z is defined to be along the beam axis) of their decay positions. High quality vertexing is also an important factor in discriminating between beauty, charm and light-quark vertices.

There must be particle identification capabilities allowing discrimination between e, μ, π, K and p over a wide kinematic range. Flavour tagging of B mesons with high efficiency and purity is only possible with good e, μ and K identification. In addition, π-K separation at around 2-4 GeV/c is necessary in order to distinguish between final states such as $B^0 \rightarrow \pi^+\pi^-$ and $B^0 \rightarrow K^\pm\pi^\mp$. There is a need for photon and π^0 detection over the range $\sim$20 MeV $<$ E $<$ $\sim$5 GeV since the final states often contain one or more π^0s. Finally, the detector should have the ability to identify neutral hadrons. This is important for reconstructing channels such as $B^0 \rightarrow J/\psi\ K^0_L$.

3.2 The PEP-II Asymmetric Collider

Perhaps the best environment in which to study CP violation in the B meson system is that provided by an asymmetric e^+e^- collider operating at the $\Upsilon(4S)$ resonance. The low Q-value

of the $\Upsilon(4S) \rightarrow B\bar{B}$ decay means that if such a collider had beams of equal energies the B mesons would be produced almost at rest. The asymmetry produces a moving center-of-mass system in the laboratory frame which allows the difference in B meson decay lengths to be measured.

To produce an asymmetric collision PEP-II uses two rings. One (the High Energy Ring or HER) contains electrons at 9 GeV and the other (the Low Energy Ring or LER) contains positrons at 3.1 GeV. This produces a relativistic boost in the laboratory frame for the resulting B mesons of $\beta\gamma = 0.56$. The electrons and positrons are injected from the SLAC[2] linac. The design luminosity of the machine is 3×10^{33} $cm^{-2}s^{-1}$.

The high luminosity and asymmetry of the PEP-II machine resulted in some unconventional design choices for the interaction region to achieve currents of the required magnitude while also reducing the machine backgrounds. The beams are bent near the interaction point(IP) since they must be brought together just before the IP and then separated again, into separate rings, before the next collision would take place. This requires strong focussing of the beams which is achieved by having quadrupoles near to the IP, and then separation of the beams by using dipole magnets. Higher levels of synchrotron radiation than are present in more conventional e^+e^- machines result from this bending of the beams. This can send off-energy beam particles and synchrotron radiation into the detector. The challenge is to achieve similar background rates to those at existing colliders while operating at an order of magnitude higher beam current than that achievable in the majority of colliders. There are three main sources of background for the detector which have been identified as synchrotron

[2]Stanford Linear Accelerator Center.

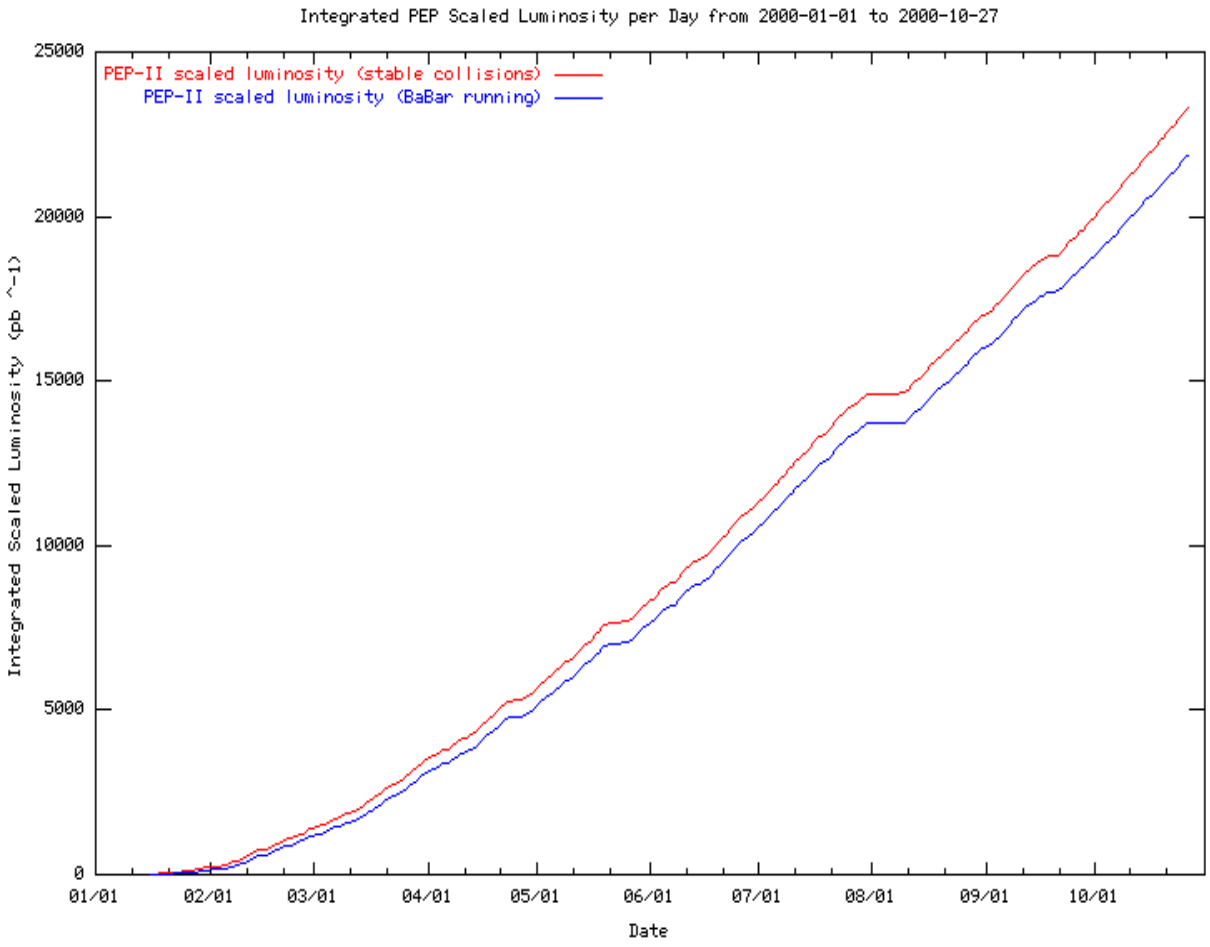

Figure 3.1: The PEP scaled luminosity integrated over the whole of the year 2000 data taking run.

radiation, lost particles due to *bremsstrahlung* with residual gas molecules and lost beam particles due to Coulomb scattering off residual gas molecules. Improving the vacuum in the beampipe will reduce the number of residual gas molecules and hence reduce the background. If the background becomes too high the detector can suffer from excessive occupancy and/or radiation damage.

The luminosity performance of PEP-II is one of the remarkable achievements to date of the B factory as a whole. During the latest run PEP-II has been setting new peak luminosity records on a regular basis (at time of writing the highest achieved is 3×10^{33} $\mathrm{cm}^{-2}\mathrm{s}^{-1}$), sometimes even surpassing the previous best on the very next shift. In addition to this, the integrated luminosity delivered by PEP-II has recently passed 25 fb^{-1}. Plans are afoot to achieve even higher luminosities in upcoming runs. Figure 3.1 shows the integrated scaled luminosity as a function of the date for data taking at BaBar throughout the year 2000. We see a steady increase during the whole year with brief plateaus in the plot corresponding to shutdown times.

3.3 Detector Overview

The BaBar detector was designed and constructed in such a way as to fulfill all the requirements mentioned in section 3.1. A cutaway picture of the detector is shown in figure 3.2. The detector can be isolated into six main subsystems (which we have numbered by their radial position from the interaction point):

1. The Silicon Vertex Tracker(SVT), which provides very accurate position information for charged tracks. In addition it is the only tracking device for charged particles with very

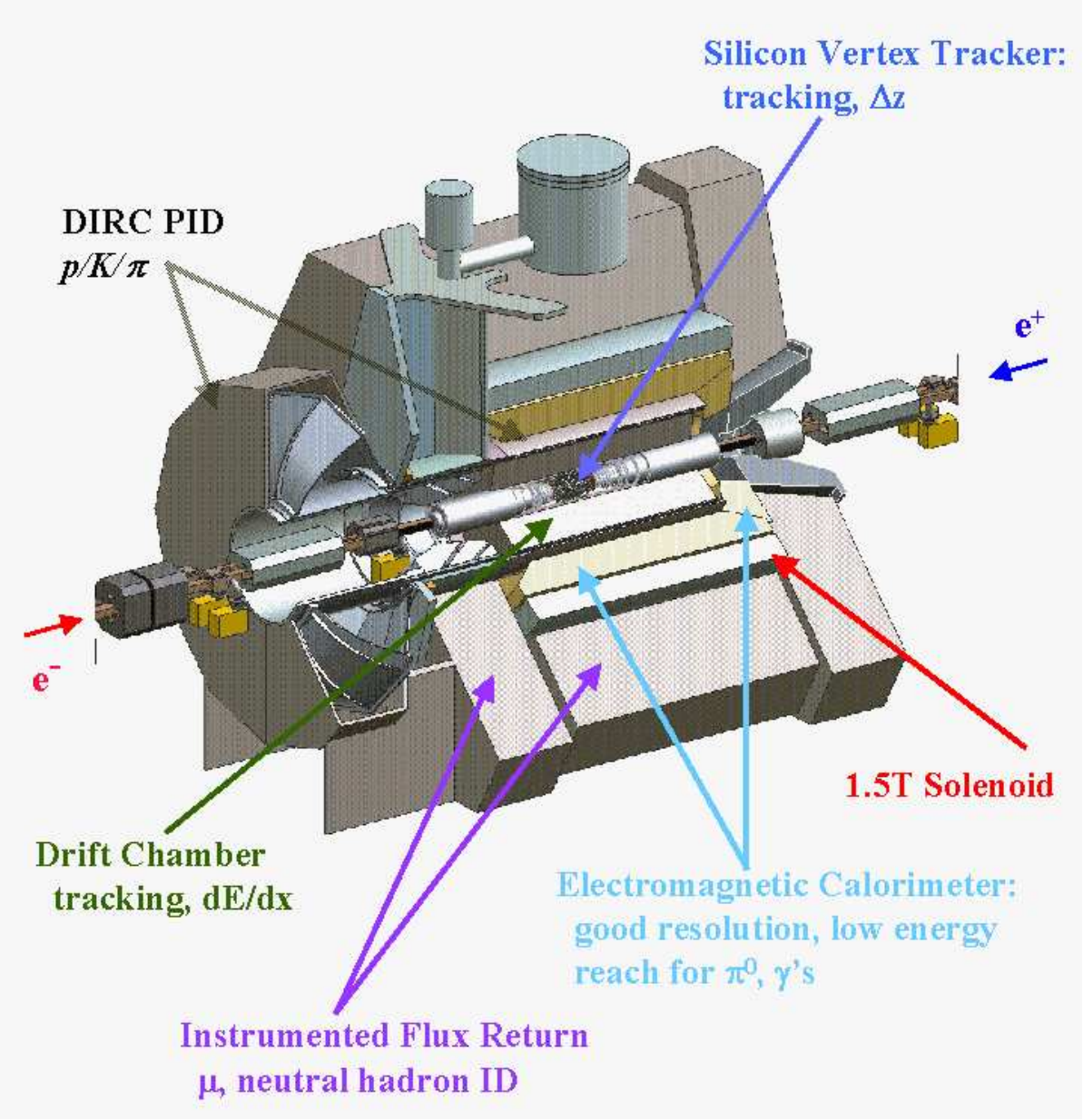

Figure 3.2: A view of the BaBar detector, see text for further information.

low transverse momentum.

2. The Drift Chamber(DCH), which has a helium based gas mixture in order to minimize multiple scattering. It provides the main momentum measurement for charged particles and also contributes particle identification information through dE/dx.

3. The Detector of Internally Reflected Čerenkov light(DIRC), which is optimized for charged hadron particle identification.

4. The Electromagnetic Calorimeter(EMC), which consists of Caesium Iodide crystals. In addition to detecting neutral electromagnetic particles it provides electron identification and information for neutral hadron identification.

5. The superconducting solenoid, which produces a 1.5 T magnetic field.

6. The Instrumented Flux Return(IFR), which provides muon and neutral hadron identification.

The next few sections will describe in detail the individual detector components.

3.4 The Silicon Vertex Tracker

The main aim of the BaBar vertex detector is to reconstruct the B meson decay vertices so that the time difference between them can be measured. This in turn is necessary for a measurement of CP violation to be made. The innermost points on a track, which are measured by the SVT, provide the most accurate measure of the track angles ϕ and θ as well

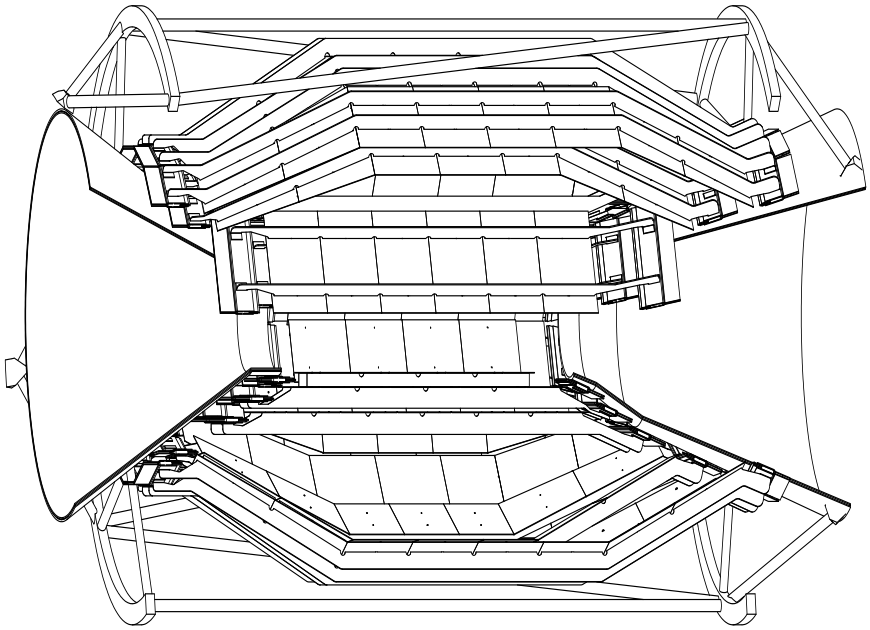

Figure 3.3: A three-dimensional cutaway view of the BaBar silicon vertex tracker.

as the x-y impact parameter with respect to the interaction point. In addition, the SVT is solely responsible for tracking charged particles with $P_t < 100$ MeV/c.

At PEP-II the mean value of the separation of the B vertices is $\sim$ 250 μm. A single vertex resolution of better than 80 μm is required to resolve the two B decay vertices. This is well within the capabilities of modern silicon microstrip detectors. The multiple scattering in the beam pipe, and in the silicon itself, sets a lower limit on the useful intrinsic resolution. The inner layers achieve a point resolution of 10-15 μm and the outer layers 30-40 μm. Also, the SVT needs to cover the largest possible solid angle for acceptance. Limitations on this are set by the dipole bending magnets placed close to the interaction point and various support structures and electronics. The polar angle coverage is from 20.1° to 150.2°.

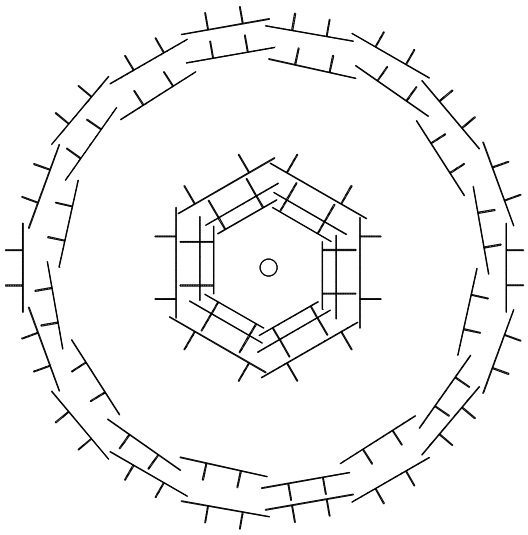

Figure 3.4: A cross-sectional view of the SVT in the plane perpendicular to the beam axis. The lines perpendicular to the detectors represent structural beams.

The SVT has 5 layers of silicon microstrip detectors. The inner two layers are the most important for the impact parameter measurements since they are the closest to the interaction point. They should have good point resolution and a high efficiency. The outer two layers are useful for alignment with tracks detected in the drift chamber (see next section). The middle layer gives extra tracking information particularly for charged particles that do not reach the drift chamber. Studies were carried out to determine how best to optimize the resolution of the different layers and can be found in [12, 13].

The SVT consists of five concentric cylindrical layers of double-sided silicon detectors. Each layer is divided around the azimuthal angle into modules. The inner three layers have six modules each, in a barrel arrangement. The outer two layers have 16 and 18 modules respectively and form an arch structure. This feature increases the solid angle coverage and avoids large track incidence angles. Each module is divided into forward and backward

half-modules which are kept electrically isolated from one another. Half-modules contain between two and four detectors. The inner sides of the detectors have strips which are oriented perpendicular to the beam direction to measure the z coordinate. The outer sides have strips orthogonal to the z strips to measure the ϕ coordinate. In total there are 340 silicon detectors covering an area of ~ 1 m^2 and about 150,000 readout channels. Figures 3.3 and 3.4 show schematic views of the silicon vertex tracker.

3.5 The Drift Chamber

The BaBar drift chamber is the main tracking device of the detector. It has a high efficiency for charged tracks with a transverse momentum of greater than 100 MeV/c. It provides a spatial resolution of better than 140 μm and a dE/dx measurement with a resolution of 7%. For tracks with $P_t > 1$ GeV/c the momentum resolution is $\sigma_{P_t}/P_t \approx 0.3\%$. The tracking coverage/$4\pi$ is 0.92. In addition the DCH serves as one of the principle triggers[3] for the experiment. Since the material in the DCH affects the performance of the DIRC and the electromagnetic calorimeter, it was built using lightweight materials and uses a helium-based gas mixture. The readout electronics are mounted on the rear endplate in order to reduce the amount of material in the forward region (since the distribution of tracks will be biased toward the forward region we want to have as little material there as possible). A more detailed description can be found elsewhere [14].

The BaBar drift chamber is a 280 cm long cylinder with an inner radius of 23.6 cm and an outer radius of 80.9 cm. The endplates are made of aluminium with the forward endplate

[3]We discuss what is meant by a trigger in section 3.9

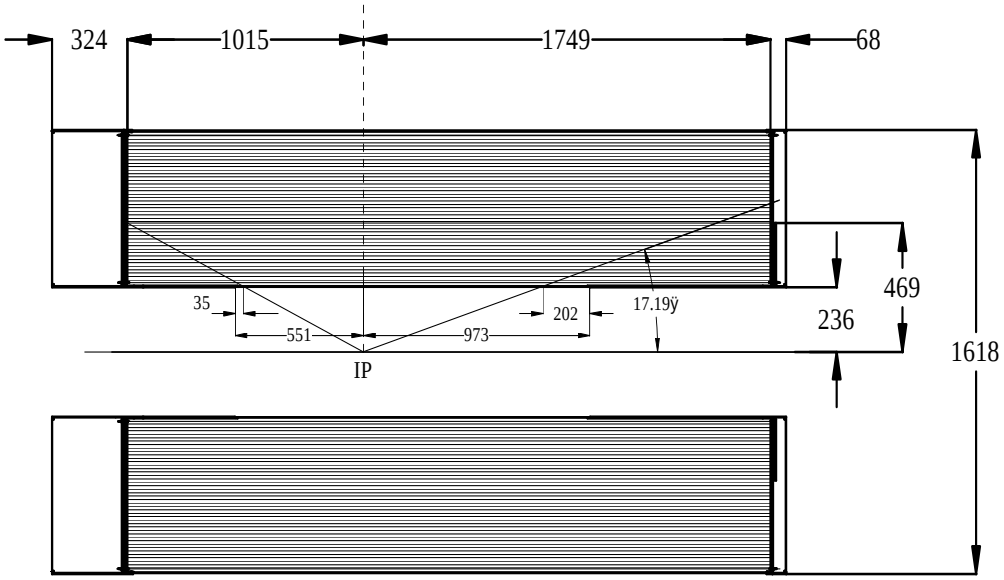

Figure 3.5: A side view of the BaBar drift chamber (the dimensions are expressed in mm).

being half as thick as the rear one at 12 mm. The inner cylinder is 1 mm or 0.28% X_0 of beryllium and the outer cylinder consists of two layers of carbon fiber on a Nomex core, corresponding to 1.5% X_0. Figure 3.5 shows a schematic side view of the drift chamber.

There are 7104 hexagonal drift cells with a typical dimension of 1.2 x 1.8 cm^2. They are arranged in 10 superlayers each consisting of 4 layers. Axial(A) and stereo(U,V) superlayers alternate according to the pattern shown in figure 3.6. The angle of the stereo wires, with respect to the axis of the chamber, varies from 40 mr in the innermost stereo superlayer to 70 mr in the outermost stereo superlayer.

The sense wires are 20 μm gold-plated tungsten-rhenium and carry 1960 V (although some data were recorded with 1900 V). The field wires are 120 μm and 80 μm gold-plated aluminium. The field-shaping wires at the boundaries of the superlayers carry 340V and other field wires are connected to ground. The gas mixture is helium-isobutane (80%:20%)

and is chosen to provide good spatial resolution and dE/dx resolution with a short drift time while minimizing the amount of material present. The gas and wires correspond to 0.3% X_0 for a track at 90° [15]

When a particle passes through the BaBar drift chamber the gas in the chamber is ionized and the time for liberated electrons to drift from the production point to the anode is measured. This time is transformed into a drift-distance by using the drift-velocity of the electrons. The signal measured on the wires is amplified due to avalanche multiplication in the gas prior to reaching the detection wires. Each initial ionized electron produces on the order of $10^4 - 10^5$ electrons, hence enabling the problem of electronic noise to be overcome. When measuring drift-time, the electronics looks for the leading edge of the signal from the charge that arrived at the sense wire. The time is then digitized with a resolution of 1 ns. For dE/dx measurements, the total charge in the pulse is summed. A requirement of the BaBar DCH electronics is to not degrade the intrinsic resolution of the chamber by more than 10%.

The amplifier, digitizer and trigger interface electronics are mounted on the rear endplate of the drift chamber, in water-cooled aluminium boxes. The electronics provides trigger information by sending the data from all the 7104 channels to the level 1 trigger system with a sampling frequency of 3.75 MHz. The system is designed to maintain good performance even in the presence of high backgrounds with a single-cell efficiency for the trigger signal of greater than 95%.

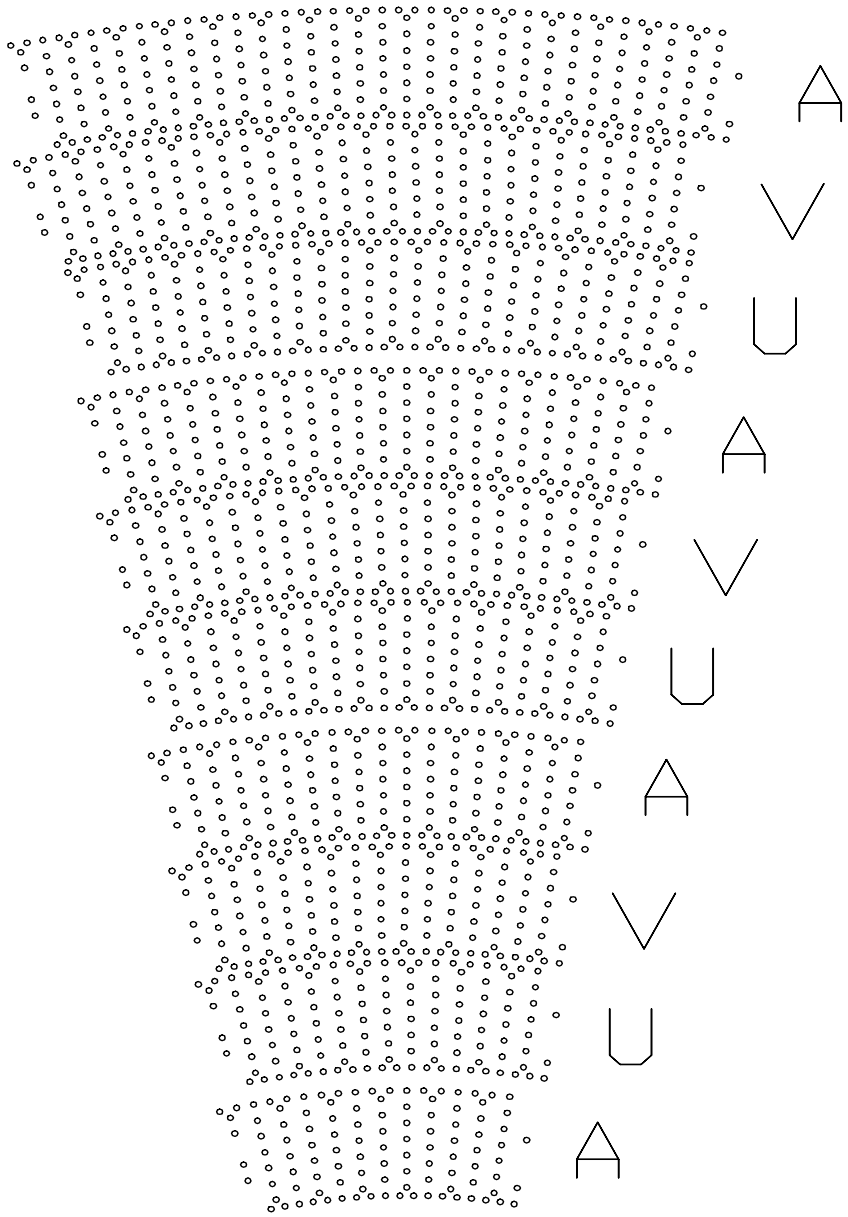

Figure 3.6: Arrangement of superlayers in BaBar drift chamber.

3.6 The DIRC

The DIRC, Detector for Internally Reflected Čerenkov light, is a new type of particle identification(PID) device. The PID requirements of the BaBar experiment are based around the need to tag the flavour of B meson decays, and to distinguish between different decay channels. To satisfy the tagging requirement, the DIRC must provide excellent kaon and pion identification up to momenta of about 4 GeV/c. The need to distinguish between different states is important in rare decays used to measure the CP angles. In addition to good K/π discrimination the DIRC may assist in muon identification in the range where the IFR is inefficient, below $\sim$ 750 MeV/c.

The concept of the DIRC is the inverse of that for traditional ring-imaging Čerenkov counters (RICH) in that it relies on photons that are trapped in the radiator through total internal reflection. A Čerenkov photon will typically undergo approximately 200 'bounces' within the quartz [16], the actual number being dependent on the dip angle of the track and hence the photon angle in the quartz, and independent of particle type to a good approximation [17]. The Čerenkov radiation is emitted at a well known angle with respect to the track direction, namely $\theta_c = \arccos(1/\beta n)$ where n is the refractive index of the radiator medium.

The DIRC radiator consists of 144 bars of synthetic quartz arranged in a 12-sided polygonal barrel shape. The quartz extends through the magnet flux return in the backward direction in order to bring the Čerenkov light outside the tracking and magnetic field volumes. All of the readout happens at this end in order to help reduce the amount of material

in the forward direction. The forward end has mirrors at the ends of the bars which reflect light back towards the instrumented end.

The DIRC occupies only 8 cm of radial space and represents 14% of an X_0 for a particle at 90° [9]. The design aims to minimize the effect of the DIRC on the calorimeter behind it. Coverage in the polar angle in the center-of-mass frame is 87% and in the azimuthal angle it is 93%.

Before detection the Čerenkov image is allowed to expand in a tank of purified water whose refractive index matches well that of the quartz bars (for which n=1.474). At the far end of the tank is an array of photomultiplier tubes (PMTs) lying on a surface which is approximately toroidal so as to make the photon path length constant at 1.2 m over a large angular range. The backward end of each bar has a small, trapezoidal piece of quartz glued to it. This allows for a reduction in the number of PMTs required by folding one half of the image onto the other half and also reflecting photons with large angles in the radial direction back into the detection array. There are about 11,000 PMTs and the standoff box is filled with 6 m^3 of water.

The difference in Čerenkov angle between a pion and a kaon at 4 GeV is about 6.5 mr. This requires the Čerenkov angle of a track to be resolved to 2 mr or better to achieve good K/π separation. This is achievable given a single photoelectron resolution of the order of 9 mr and between 25 and 50 photoelectrons per track [9].

3.7 The Electromagnetic Calorimeter

The physics that the BaBar experiment has been designed to study requires excellent electromagnetic calorimetry. On average generic B decays contain 5.5 photons with about half of the photon energies below 200 MeV [18]. This causes the π^0 and B reconstruction efficiencies to fall off very quickly as the minimum detectable photon energy increases. In addition many of the B decays used to study CP violation contain at least one π^0 and have characteristically small branching ratios. Thus, high efficiency for low energy photons along with good energy and angular resolution is required to accurately reconstruct these states and improve their signal-to-background ratios. The calorimeter also facilitates lepton identification by providing e/π and e/μ separation and therefore provides one of the B flavour tags required by all CP analyses.

The BaBar calorimeter uses a quasi-projective arrangement of crystals made from Thalium doped Caesium Iodide covering a range of center-of-mass solid angle for photons of -0.916 $\leq \cos\theta \leq$ 0.895. The crystals are divided up into two main sections, the barrel and the forward endcap. There are 5760 barrel crystals, arranged in 48 theta rows, each row having 120 identical crystals around ϕ. The length of the crystals varies from 29.76 cm (16.1 X_0) at the rear of the barrel to 32.55 cm (17.6 X_0) at the front.

3.8 The Instrumented Flux Return

The outermost detector in BaBar consists of layers of resistive plate chambers (RPCs) which use the iron of the magnet return yoke as an absorber. It is optimized for the identification of muons and the detection of neutral hadrons. The IFR consists of a barrel section and

forward and backward endcaps. The endcaps allow the solid angle coverage to go down to 300 mr in the forward direction and 400 mr in the backward direction.

The graded segmentation of the iron, which varies from 2 cm to 10 cm is a novel feature of the experiment. It allows for both improved muon identification at low momenta and better K_L^0 detection.

3.9 The Trigger System

The purpose of the BaBar trigger system is to select interesting physics events, with a high and well known efficiency, for mass storage. The two main components are Level 1, which runs in hardware and Level 3, which is implemented in software. From the PEP-II beam crossing rate of 238 MHz, the Level 1 trigger must accept events no faster than 2 KHz, as required by the data acquisition system.

The data for the Level 1 trigger comes from two different subdetectors of BaBar - the drift chamber (which is sensitive to charged tracks) and the electromagnetic calorimeter (which is sensitive to charged tracks and photons). This information is then passed to a global trigger, which also uses information from the IFR to veto cosmic ray events. Using two independent systems has great advantages - the trigger will be more reliable and each can be used to check the other.

The Level 3 trigger (or L3) contains a flexible combination of tools to reduce backgrounds while keeping the interesting physics events. L3 is designed to further reduce the rate to no more than 120 Hz at design luminosity. This is achieved by using a hierarchy of algorithms, which are constructed from a set of filters and tools so that the decision of whether to keep

an event can be made as quickly as possible. L3 then categorizes events into topological families and applies rules to these families to determine whether to log events [19]. In Level 3, the rates of all physics processes (except for $e^+e^- \to e^+e^-$) amount to about 20 Hz of the 120 Hz budget at design luminosity.

With the PEP-II beam crossing rate of 4.2 ns it is impossible to tell, in real time, which beam crossing an event came from. Therefore we use information from the reconstruction to determine this. Using segments found independently in each drift chamber superlayer one can relate the measured delta T0 to the time of the interaction producing the particle, accounting for the time of flight of the particle. The resulting resolution on the collision time is ~ 1 ns for multi-hadron events.

Chapter 4

Track Fitting and Hypothesis Testing

4.1 Introduction

When proceeding to fit a trajectory one is aiming to determine a set of parameters and to test the trajectory hypothesis. The primary focus of this section will be on the hypothesis testing aspect of track fitting.

In the BaBar tracking volume we obtain measurements in the form of hits on the silicon wafers in the SVT, and the wires in the DCH. From these we then reconstruct the tracks and, test the hypothesis that the particular set of hits is validly described by the parameterised trajectory. The methodology behind this can be thought of in two distinct parts, 'track finding' and 'track fitting'. Track finding seeks to recognise patterns among the hits in an event; once a pattern is distinguished the track fitting algorithms are then run to reconstruct the path taken by the particle that is thought to have yielded that set of hits and to test the consistency of the hits with the fitted trajectory. Herein, a simple track fitting algorithm will be described and then improvements on this which lead to the BaBar Kalman Filter, the track fitting algorithm used in BaBar, will be discussed.

4.2 Fitting Techniques

When charged particles pass through an axial magnetic field, along the z axis, the trajectories formed are helical. These trajectories can then be factored into two separate parts, a circle defined in the x-y plane and a straight line in the s-z plane, s being the distance travelled from the point-of-closest approach to the origin. Splitting this helix into two separate parts simplifies the track fitting somewhat and results in no loss of information if the x-y and s-z measurements are independent. In BaBar, this is not the case since the stereo wires of the drift chamber couple z and r-ϕ information. However, in the simplified Monte Carlo simulation that was generated to examine the hypothesis tests (see section 5.1) the track fit was separated into x-y and s-z fits and only the x-y fit was used in the evaluation of hypothesis tests.

4.2.1 Least-squares Fit

The least-squares technique involves minimizing a sum of squared differences between the data and expectation, usually with some error measure (or weight factor) specified. Suppose there are a set of N measurment points, x_i, where the i^{th} measurement y_i is assumed to be chosen from a Gaussian distribution where $F(x_i; a)$ is the mean and σ_i^2 the variance. χ^2 can be written as,

$$\chi^2 = \sum_i^N \frac{[y_i - F(x_i; a)]^2}{\sigma_i^2}. \tag{4.1}$$

If the theory prediction is a function which is linear in the κ unknown parameters a, we can write it as,

$$F(x_i; a) = \sum_{\mu=1}^{\kappa} a_\mu f_\mu(x_i). \tag{4.2}$$

where the f_μ are κ linearly independent functions, which are single valued over the allowed range of x. Using the definitions,

$$g_\mu = \sum_i^N \frac{y_i f_\mu(x_i)}{\sigma_i^2} \tag{4.3}$$

and

$$V_{\mu\nu}^{-1} = \sum_i^N \frac{f_\nu(x_i) f_\mu(x_i)}{\sigma_i^2}, \tag{4.4}$$

the parameters, a, that minimize χ^2 by setting $\frac{\partial \chi^2}{\partial a_\mu} = 0$, for all κ can be found. This minimum value of χ^2, denoted as χ^2_{min}, then allows one to test how probable the data were given the theoretical hypothesis. The probability of acquiring a χ^2_{min} value at least as large as the one obtained is then given by the integral distribution of χ^2 for n degrees of freedom, where $n = N - \kappa$.

A more general definition of equation 4.1 arises when considering that the measured y_i's are not independent, and one must consider them as coming from a multivariate distribution with a non-diagonal covariance matrix, S. This generalization can be written as,

$$\chi^2 = \sum_{ij} [y_i - F(x_i; a)] S_{ij}^{-1} [y_j - F(x_j; a)]. \tag{4.5}$$

The extended definitions of equations 4.3 and 4.4 can then be written as,

$$g_\mu = \sum_{ij} y_i f_\mu(x_j) S_{ij}^{-1}, \tag{4.6}$$

and

$$V_{\mu\nu}^{-1} = \sum_{ij} f_\nu(x_i) f_\mu(x_j) S_{ij}^{-1}. \tag{4.7}$$

The construction of the covariance matrix, S, is simplified in that the contributions to S are additive. However, since S^{-1} is required there is still an expensive matrix inversion which must take place.

χ^2 can be rewritten in the compact form,

$$\chi^2 = \Delta^T S^{-1} \Delta, \tag{4.8}$$

where Δ is the difference between the track parameter measurements (y_i) and the actual parameterized trajectory ($F(x_i; a)$) and S is the covariance matrix of errors. The elements on the principal diagonal of the covariance matrix are σ_{ii} where $i = 1, 2, ..., N$, N corresponding to the total number of hits used in the initial fitted trajectory and the σ corresponding to the variances of the individual measurements. The off-diagonal elements are the covariances σ_{ij} (where $i \neq j$) of the variables we measure.

4.2.2 Kalman Fitting

The Kalman filter is well established as the standard formalism for fitting tracks in high-energy physics experiments [20, 21]. This stepwise parameter estimation technique was originally developed in the early 1960's to predict the trajectories of rockets given a set of their past positions. It can be used for our purposes to handle multiple scattering while estimating track parameters.

One fits sequentially along the trajectory extrapolating towards the next point of measurement, at each juncture including terms for multiple scattering into the covariance, and then incorporating the information contained in this new measurement. This extrapolation is normally carried out over small distances and therefore we can linearize the trajectory taken by a particle, between measurement points, without losing precision. If one pictures a particle that begins its path travelling along the x axis of some material, which produces scattering between the measurement points, then the Kalman filter solution of this would

be an average of two progressive fits, one going towards positive x and the other going towards negative x. Filtering is the estimation of the "present" state vector based upon all "past" measurements. For forward filtering, this means estimating track parameters k using measurements up to and including m_k. For backward filtering, this means estimating track parameters at k using the measurements m_N down to m_k.

In order to obtain the optimal fit parameters at a measurment point one can take the weighted average of the forward going fit, proceeding from the first measurement to the point of interest, with the backward going fit from the final point to the measurement point of interest. However, these two fits are not 'smooth' since they allow for discrete scattering angles in the material traversed. We have no information regarding the fit at the first point, but our knowledge of the trajectory increases as the fit proceeds towards the end, where all hits have been incorporated. The converse is true when fitting in the opposite direction, and so when we average the two fits a more complete description of the trajectory is obtained than by simply using one of the progressive fits.

A major improvement on the full χ^2 solution arises in the speed of the algorithm since it scales linearly with the number of measurements. However, since the Kalman filter approach is sequential, it only allows for correlations between a hit and all the subsequent hits on the trajectory. The sources of correlations are sequential, or causal. Therefore, one can structure the track fit such that it accounts for only a restricted set of correlations and hence obtain a significant improvement in performance.

For a linear problem or one with Gaussian-distributed errors the linear-Kalman filter yields the optimal solution with less computation than required to invert the full covariance

matrix of the measurements. However in the presence of non-Gaussian trajectory deviations the linear Kalman filter may not perform as well as a non-linear filter.

4.2.3 Track Finding and Fitting in BaBar

Different algorithms are used for tracks found independently in the two tracking devices, the silicon vertex tracker and the drift chamber. The SVT algorithm starts by combining r-ϕ and z hits in the same silicon wafer to form space points, and then employs an exhaustive search for good helical tracks, requiring hits in at least four of the five layers of silicon. There are two drift chamber algorithms which are run in sequence. The first finds straight line track segments in all ten superlayers. Segments are then combined to form first a circular track (which uses only the axial segments and has a strong bias towards tracks coming from the interaction point), and then a helical track (by combining information from the stereo segments to the axial tracks). The second drift chamber track-finding algorithm uses circular segments in three adjacent superlayers (all eight possibilities are tried) to form a trial helix. If this helix is of sufficient quality, it is projected forward and backward, and other segments are added to it. This second algorithm is designed with those tracks not coming from the primary vertex in mind, tracks only passing through a small number of superlayers (tracks with a large dip angle) and low P_t tracks. Another algorithm is designed to merge the separately found drift chamber and silicon vertex tracks, projecting each silicon vertex and drift chamber track into the support tube and looking for good matches. Those that match are combined into a single track.

Initially, all tracks are fitted with a simple helix fitter (i.e. a least-squares fit with a

diagonal covariance matrix, which corresponds to a simple χ^2 fit). The hit which contributes the most to the χ^2 is removed. This procedure is iterated until all surviving hits give $\chi^2 < \chi^2_{max}$, where χ^2_{max} is typically chosen to be 9. Essentially we throw away the hit with the largest pull[1] and then refit with $N-1$ hits. This iterative hit discarding is carried out to remove noise hits and hits which are a bad match for the fitted trajectory. A more thorough explanation of this procedure can be found in [5, 22, 23]. The residuals[2] to the fit contain useful information regarding the resolution and systematic bias of the measurements and the validity of the trajectory hypothesis.

After merging the drift chamber and silicon vertex tracks, the merged tracks are assigned track parameters based on a weighted average of the two input tracks. All of the tracks in the output list are then refit with the Kalman filter fitter. The way in which BaBar implements the Kalman filter uses a novel formulation of the processing equations which is well suited to Object Oriented programming [24]. The formulation produces, along the full particle trajectory, optimal track parameters for all five stable charged particle mass hypotheses (e, μ, π, K, p). A more thorough description of the BaBar track fitting algorithm is given elsewhere [25].

4.3 Testing Hypotheses

Once a track has been fit we should then be able to use it to perform our physics analyses. However, before this is done we want to ensure that each track that has been fit is a good

[1] Essentially the normalized residual, or the residual(see footnote 2) divided by the uncertainty assigned to that measurement.

[2] Where the term residual refers to the signed distance of closest approach between a measurement and the fitted trajectory.

match to the measurements used in that fit and test the trajectory hypothesis. This section will go on to describe how this is traditionally done (in section 4.3.1) and how improvements can be made on this standard procedure (in section 4.3.2). Searching for badly fitted tracks or "kink-finding" [26] as it is commonly referred to in BaBar falls naturally into two categories: 1) Searching for kinks within a single reconstructed track and 2) Searching through pairs of reconstructed tracks for kinks. This study will only be concerned with the case where the kinks are found in single tracks.

One cause of track deviations is the decay-in-flight of the parent particle to one or more daughter particles. A decay such as $\pi^+ \rightarrow \ \mu^+\nu_\mu$(+ charge conjugate), which we want to eliminate from providing a fake muon signal, would usually be fit as a single track in the momentum range in which we are interested (since the rest mass of the pion and muon are relatively close). However, a decay such as $K^+ \rightarrow \ \mu^+\nu_\mu$(+ charge conjugate) would often be measured as two separate tracks since when the heavier kaon decays to a muon there is a larger deviation in the path. Although connected through their physics processes these are essentially two independent issues and as such are treated that way. Improving fake track rejection is therefore the aim of both 1-track and 2-track kink-finding, hence we wish to improve the efficiency with which we can find anomalous trajectory fits and increase the purity of the unkinked track samples we define.

For this analysis we concentrate solely on the 1-track kink-finding problem and issues associated with it. The decay-in-flight is not the only way in which track deviations may arise in the BaBar tracking volume. Mis-alignment errors, hard multiple scattering, *brems-strahlung* and incorrect corrections for continuous energy loss may cause a fitted trajectory

to exhibit deviations from the actual path taken. If one is purely trying to use kink-finding to improve the tracking sample then the process by which a trajectory deviation arises is not necessarily of interest (or indeed the position at which that deviation occurred). Acknowledging that the track has a discrepancy associated with it and either not using that track, or applying some extensive refit to account for the fact that the track is kinked must be done. Therefore we want to find these erroneous tracks as effectively, and efficiently as possible, so that we may then make a decision as to what will be done with them.

4.3.1 Standard Tools Used

In section 4.2.1 we discussed the uses of χ^2 in trajectory fitting and the determination of parameters arising from the fit. Minimizing the value of χ^2 also generally serves as a test of the validity of the trajectory hypothesis with the value of χ^2 at the minimum being used to test the suitability of the chosen hypothesis.

4.3.2 Improving discrimination

We are attempting to find if we can improve the sensitivity to correlations that the simple χ^2 test explicitly ignores. Correlations that are known in advance can be incorporated into a properly designed χ^2. However, it is still pertinent to perform a correlation test on the residuals to the fit to see whether the observed correlations are consistent with those assumed in the fit since χ^2 does not test for correlations amongst residuals. For the trajectory deviations we are looking to find, there would be no way to know before they were originally fit that anomalies existed and so incorporating these correlations into a prior definition would be impossible. χ^2 is not very sensitive to such mistakes if the deviation is small when

compared with measurement errors.

We will use information on correlations amongst residuals when defining variables and, in doing so, attempt to use all of the information available to us to look for poorly fitted tracks. We go on to define variables in the following section that can test whether correlations between measurements are correctly accounted for in the fitted trajectory.

4.4 Correlation Variables

Correlations among the residuals, if indeed present, may indicate that the assumed trajectory is an inadequate parameterization of the actual path taken. We will go on to discuss various ways in which deviations in fitted trajectories were tested and the variables which were used to exploit these deviations.

4.4.1 Run Test Variable

Correlations may arise in the relative signs of residuals of adjacent hits i.e. whether they appear on the same side of the trajectory or on opposite sides. The fact that only the sign of the residual is used maintains an independence between any variable defined to take account of this property and the χ^2 variable. A run test utilises the sequential correlations in the signs of fitted residuals along the flight path to form a test statistic. The length of a run is given by the number of consecutive hits on the same side of the trajectory. One could picture a simple (but as it turns out rather insensitive and ineffective) run test to be given by counting the total number of runs in the trajectory. If a deviation in the actual trajectory occurred, but an undeviated track fit hypothesis was attempted, there would be a grouping of longer runs located along this track causing the total number of runs to be less than if

a track was fit to its correct hypothesis. A more sensitive test should include information regarding the lengths of the runs, in particular the longest runs along the trajectory.

The run test variable used is defined by,

$$u = \frac{M}{\sum_{i=1}^{M} w_i} \tag{4.9}$$

where the sum is taken over the set of runs, each of which is assigned a weight w_i. The total number of runs along the trajectory is M. A simple initial choice for w_i is $2^{L(i)}$, where L(i) denotes the length of run i. Improvements can be made still further by considering not only the sign of each deviation but also its rank, r(j) (that is a list of normalised residuals, $|\delta/\sigma|$, sorted in order of size from 1 to N, the smallest taking a rank value of 1 and the largest a rank of N). Using this rank instead of the actual value of δ/σ maintains an independence between the run test variable we define and the simple χ^2 from the track fit. An appropriate choice for the weighting factor was found to be

$$w_i = \prod_{j=1}^{L(i)} \left(1 + \frac{r(j)}{N}\right). \tag{4.10}$$

This gives a larger weighting to those hits which are further away from the fitted trajectory. Results using this test can be found in section 5.2.

4.4.2 Correlation Sum

The correlation sum quantifies the degree to which nearby measurements are correlated and considers the mean correlation as a function of the distance between measurements.

$$\rho_k = \sum_{i=1}^{N-k} w_{ik} \frac{2\,\delta_i\,\delta_{i+k}}{\delta_i^2 + \delta_{i+k}^2} \;/\; \sum_{i=1}^{N-k} w_{ik} \quad ; \quad w_{ik} = \frac{\delta_i^2 + \delta_{i+k}^2}{\sigma_i^2 + \sigma_{i+k}^2} \tag{4.11}$$

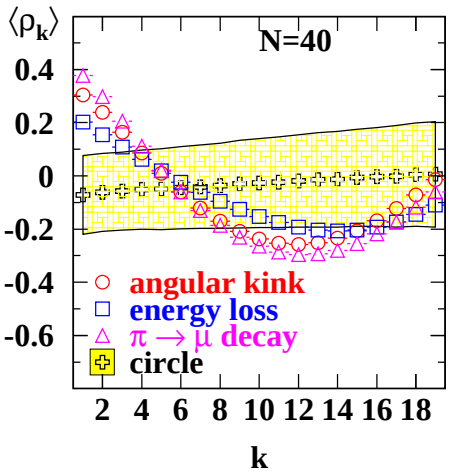

Figure 4.1: The expectation value of the correlation variable ρ_k as a function of the correlation length k. The first 19 $\langle\rho_k\rangle$ are shown for 40 measurements. Different symbols correspond to specific generated trajectories where the fitted trajectory is a circle in each case. The shaded region indicates the r.m.s. of the ρ_k distribution for the circular trajectory. This plot is taken from [27].

In equation 4.11, δ_i is the signed distance to the fitted trajectory for measurement i, k is the distance over which the correlation is taken, σ_i is the estimated uncertainty of measurement i. The weight factor given emphasizes pairs of measurements with significant deviations from the trajectory. This statistic arises from considering $(\delta_i - \delta_{i+k})^2/(\sigma_i^2 + \sigma_{i+k}^2)$ where the correlation being sought is in the actual distance from the fitted track.

This measure satisfies $|\rho_k| \leq 1$ for all k. Uncorrelated measurements should have expectation values for ρ_k that are close to zero. The introduction of slight negative correlations arise from the trajectory fit, but these are small provided the number of measurements is much greater than the number of parameters being fit. Figure 4.1 shows the expectation values of the ρ_k as a function of the correlation distance k (for k up to 19) for true circular trajectories

and three common trajectory deviations. The simulation used to generate this plot is outlined in section 5.1. The magnitudes of the $\langle \rho_k \rangle$ for each incorrect hypothesis depend on the particular choice of parameters in the simulation. We see that most of the discrimination power is concentrated at small k, since the r.m.s. of the ρ_k distribution expected for the correct hypothesis is smallest there. These considerations along with the essentially linear behaviour of the different $\langle \rho_k \rangle_{false} - \langle \rho_k \rangle_{true}$ as a function of the correlation distance k for small k/N, lead us to the following test statistic in which the ρ_k are summed with a weight that decreases linearly with k:

$$\lambda = \sum_{k=1}^{L} C_k \rho_k \text{ with } C_k = \frac{2}{L(L-1)}(L-k) \text{ and } \sum_{k=1}^{L} C_k = 1. \tag{4.12}$$

Choosing L as the nearest integer to N/8 was found to give good sensitivity to the trajectory deviations studied. This is the correlation sum variable that is used for the studies shown in sections 5.1 and 5.2. A more thorough explanation of this variable can be found elsewhere [27] (this paper is included in its entirety, with only minor alterations from the published work, in appendix A).

4.4.3 Frühwirth χ^2

Frühwirth [28] investigated a method of detecting kinks using information which is naturally given as a by-product of the Kalman filter track fit discussed in section 4.2.2. When we fit a track with N position measurements, or hits, the idea used is the following. At any hit location k, one has the best-fit track parameters (a) using all the hits 1 through k and (b) using k+1 through N. We construct a χ^2 for the consistency of these two sets of track

parameters before and after a given point on the trajectory:

$$\chi^2_{\rm match} = (\mathbf{p^B} - \mathbf{p^F})^{\mathbf{T}}[\mathbf{C^B} + \mathbf{C^F}]^{-\mathbf{1}}(\mathbf{p^B} - \mathbf{p^F}). \tag{4.13}$$

Here $\mathbf{p}$ are the forward and backward parameter vectors at some given point and $\mathbf{C}$ are the covariance matrices associated with these. The maximum value of $\chi^2_{\rm match}$ can then be used as an independent test statistic to check on the consistency of the track fit pieces, with naturally larger values occurring in this variable at sites where there is some deviation in the trajectory [29]. Since we store the full filter output when the BaBar algorithm is run there is no need for a refit to calculate this variable making it both simple and fast. However this calculation does require a matrix inversion at each possible break point tested along the track therefore making the computation required here greater than for both the run test and correlation sum calculations.

It is possible to write the χ^2 from the track fit in terms of three separate pieces :

$$\chi^2 = \chi^2_B + \chi^2_F + \chi^2_{\rm match}. \tag{4.14}$$

The terms in equation 4.14 correspond to the backward and forward parameters with a matching term between track pieces. It is this matching term that is used as a hypothesis testing variable and so it should be noted that this variable is not independent of the χ^2 from the track fit. However, both the run test variable and correlation sum are defined to be independent of the track fit χ^2.

Chapter 5

Application of Hypothesis Testing Variables

5.1 Initial Monte Carlo Studies

We began our studies on hypothesis testing independent of the BaBar detector by writing a simplified Monte Carlo simulation on which we could test our ideas. Much of what is to follow is described in further detail in [27] and appendix A. We generated a set of charged particles which were tracked through a uniform, axial magnetic field and measurement points were generated in the plane orthogonal to the field direction. The number of hits generated per particle and the hit resolution were chosen to mimic those of the BaBar drift chamber [18]. A hit efficiency of unity was used and no noise was generated. Measurement points were uniformly distributed along the trajectory and the generated points were fitted to a circle where all measurements were used in the fit i.e. perfect pattern recognition was assumed. The generated positions were also smeared by an experimental resolution and Gaussian distributed measurement uncertainties were assumed.

This provided us with the initial platform to evaluate the correlation test statistics described in sections 4.4.1 and 4.4.2. The run test variable, correlation sum (which is given

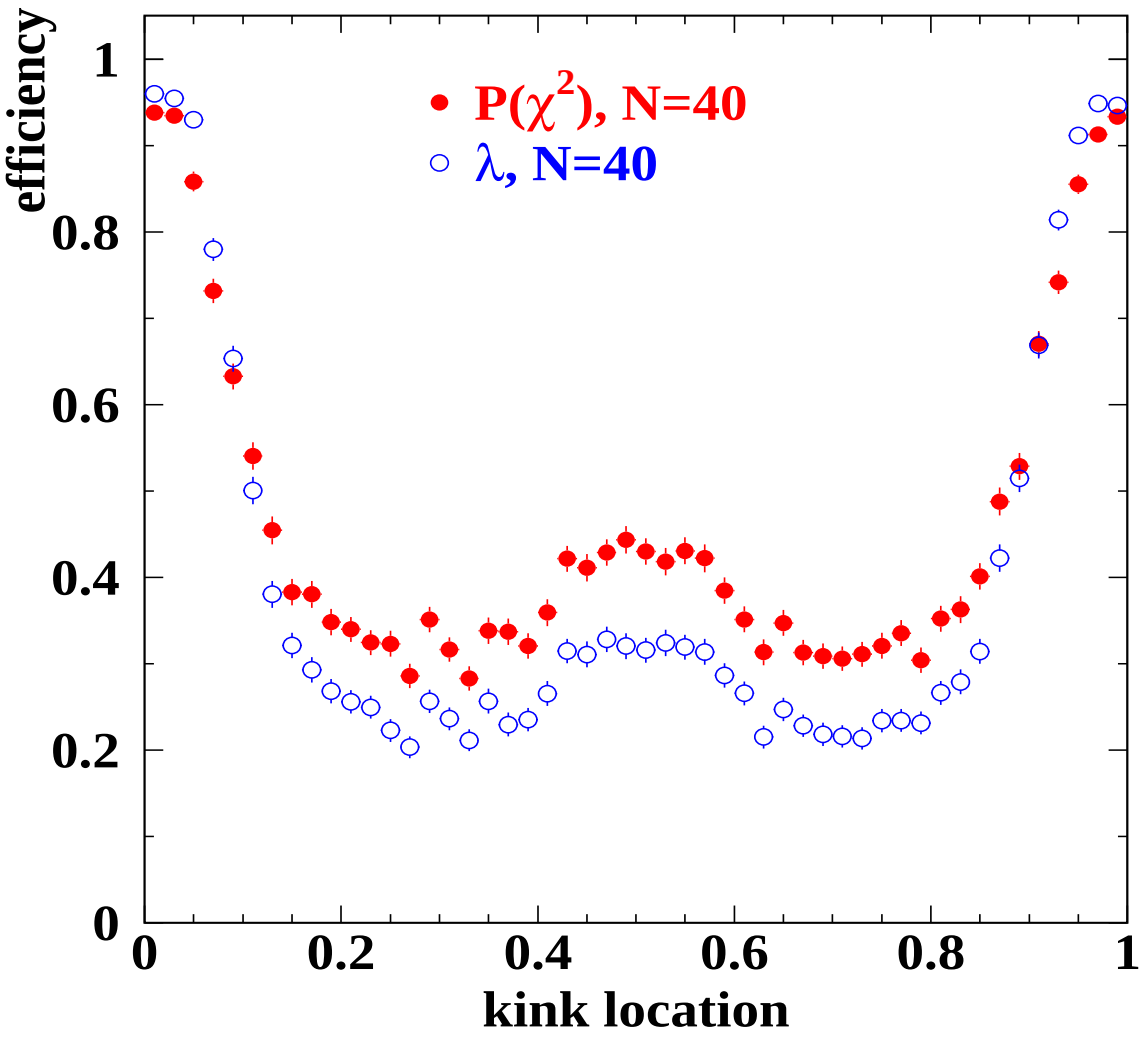

Figure 5.1: The survival rate as a function of the kink position within the measurement volume. The cuts on λ(correlation sum) and P(χ^2) give 95% efficiency for true circular trajectories. This plot is taken from [27].

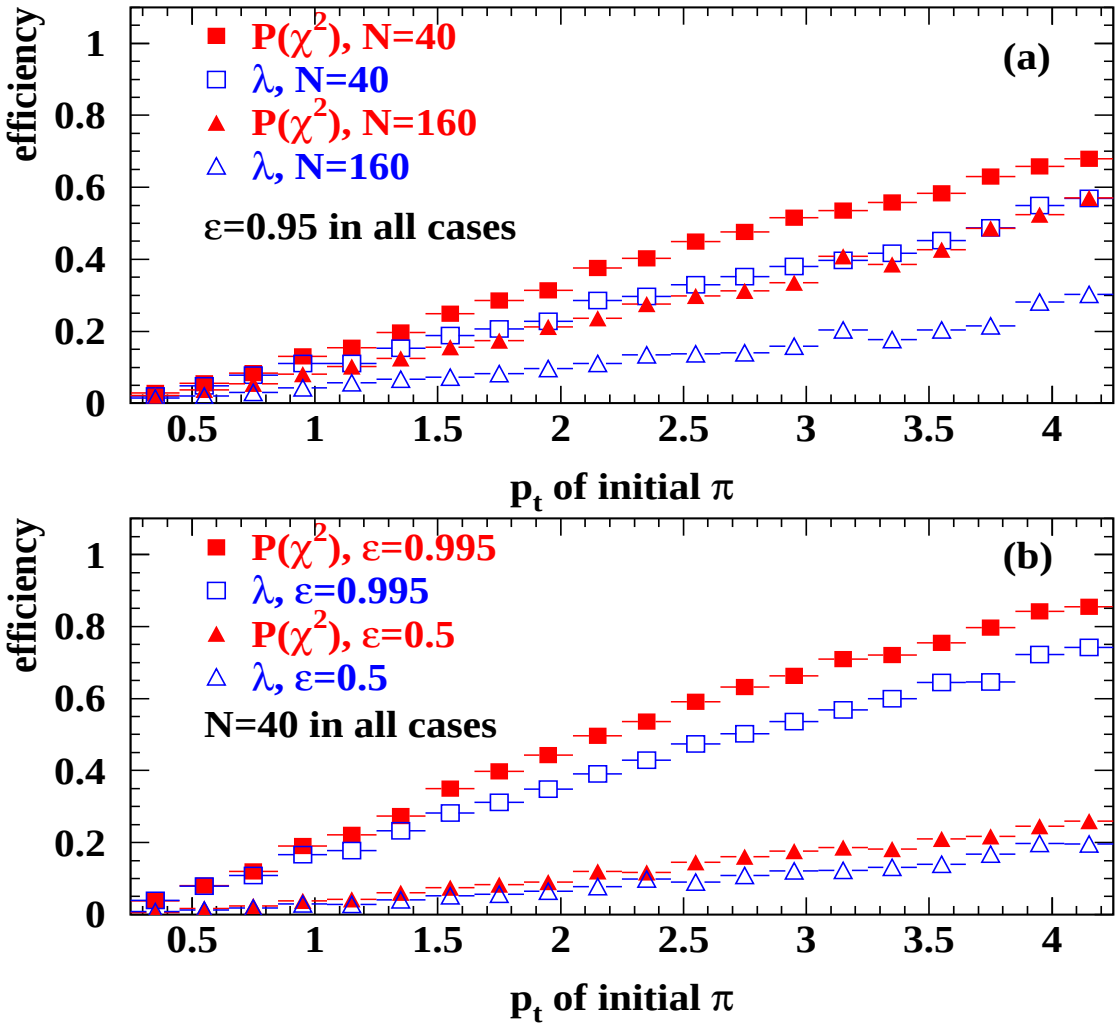

Figure 5.2: The survival rate for $\pi^+ \rightarrow \mu^+\nu_\mu$(+ charge conjugate) decays occurring as a function of the transverse momentum of the pion. The behaviour is shown for different numbers of hits, N, for (a) a cut that gives an efficiency of 95% for true circular trajectories. The curves in (b) show the effect of varying the cut on ϵ. This plot is taken from [27].

the term λ in figures 5.1 and 5.2 to match that of the definition given in section 4.4.2) and the probability of χ^2, P(χ^2), were tested using this simplified Monte Carlo simulation (the curves in figures 5.1 and 5.2 do not show results for the run test variable). It was found that the correlation sum provided superior discrimination to the run test variable and P(χ^2) for removing the generated kinked tracks. Figure 5.1 shows the fraction of trajectories surviving a cut on the correlation sum and P(χ^2) that retains 95% of the true circular tracks as a function of the position of a discrete angular kink, where the kink angle is uniformly distributed between ± 0.02 radians. As is evident from the plot, we are better able to discrepate kinked tracks from true circular trajectories within the central measurement volume.

In figure 5.2 we look at $\pi^+ \rightarrow \mu^+\nu_\mu$(+ charge conjugate) decays occurring in the fiducial region as a function of the transverse momentum of the initial pion. We see that the best rejection i.e. the lowest efficiency for incorrectly selecting these kinked tracks, is at lowest momenta, where the kink angle is largest and that rejection efficiency increases as the initial pion momentum is increased. Again we see that the correlation sum variable is a significantly better discriminant than P(χ^2). The distributions in figure 5.2(a) also show the effect that increasing the number of measurements has on the survival rate. As expected, there is an improvement in the correlation sum sensitivity to kinks when there are more measurement points. The physical correlation length sampled by the correlation sum is about 1/8 the length of the track, hence, increasing the density of the measurements allows a more precise determination of the correlation.

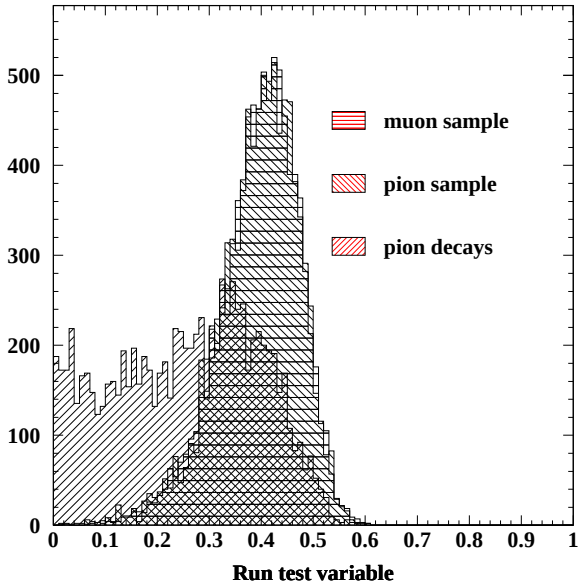

Figure 5.3: Run test variable for both decayed and undecayed particles. A more complete description is given in the text.

5.2 Results from the BaBar Monte Carlo

Having examined the correlation sum variable in our simplified Monte Carlo simulation, we evaluated these variables using the full BaBar Monte Carlo. A 1-track kink-finding module was created to accomodate the set of kink finding algorithms used[1]. This module was run at the end of the track reconstruction sequence after all of the DCH and SVT pattern recognition and track fitting (which was mentioned earlier) had been completed. In this respect we could take advantage of the full SVT-DCH tracking volume and our kink finding effort was not restricted to one particular subsystem. However, utilising the two subdetectors implicitly relies on good alignment between them.

Figures 5.3, 5.4, 5.5 and 5.6 show the distributions for both kinked and unkinked tracks

[1]The implementation of this kink-finding module in BaBar was carried out by Justin Albert of Princeton University.

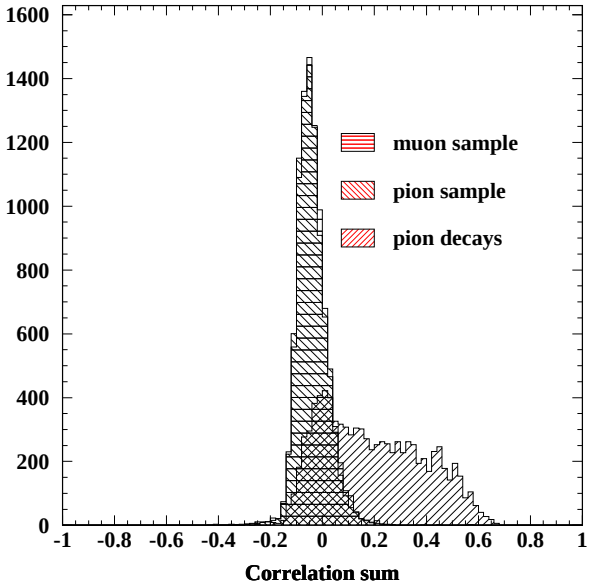

Figure 5.4: Correlation sum for both decayed and undecayed particles. A more complete description is given in the text.

using the run test variable, correlation sum, Frühwirth(χ^2) and P(χ^2) respectively. Both a single muon sample and single pion sample (with 100x reduced lifetime for increased chances of decays) are presented. The muon sample refers to single generated muons, pion sample to those pions that remain undecayed and pion decays are those pions which have decayed to muons between the 5th hit and 5th-from-last hit on the track. All plots are normalised such that the three distributions contain the same number of events.

One can see that both the muons and undecayed pions lie almost on top of one another in these plots. Therefore we show that all four variables give good agreement for single particle species tracks, even if the species itself differs. There is a clear region of discrimination between kinked and unkinked tracks which is noticeable in each of the four plots. These differences allow us to discriminate $\pi^+ \rightarrow \mu^+\nu_\mu$(+ charge conjugate) decays from undecayed tracks.

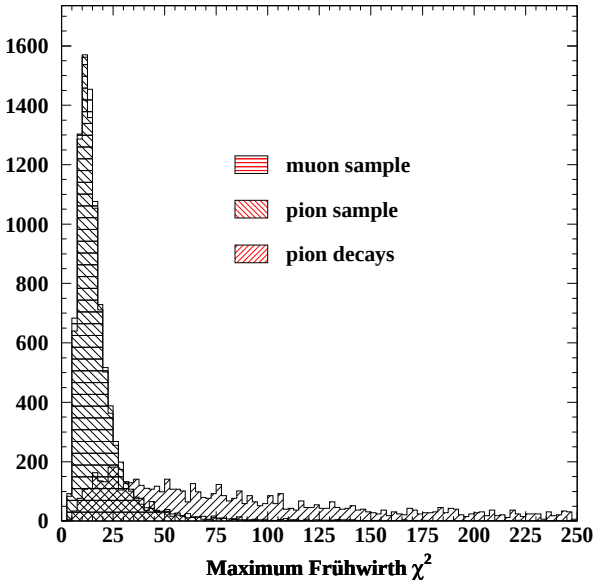

Figure 5.5: Frühwirth(χ^2) for both decayed and undecayed particles. A more complete description is given in the text.

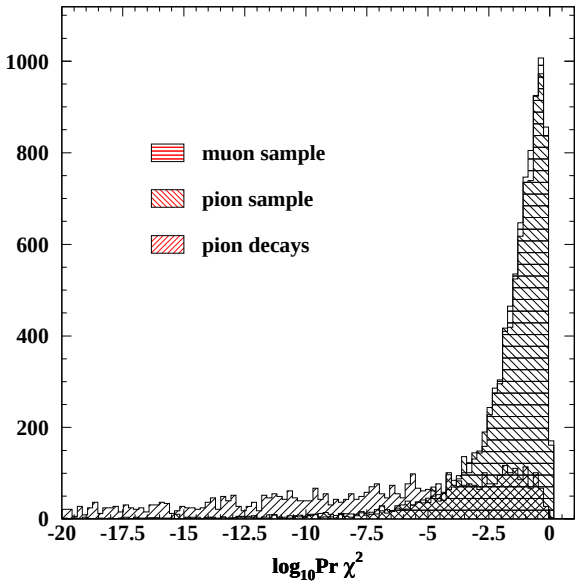

Figure 5.6: P(χ^2) for both decayed and undecayed particles. We plot $\log_{10}$ of P(χ^2) to emphasize the peak near zero probability. A more complete description is given in the text.

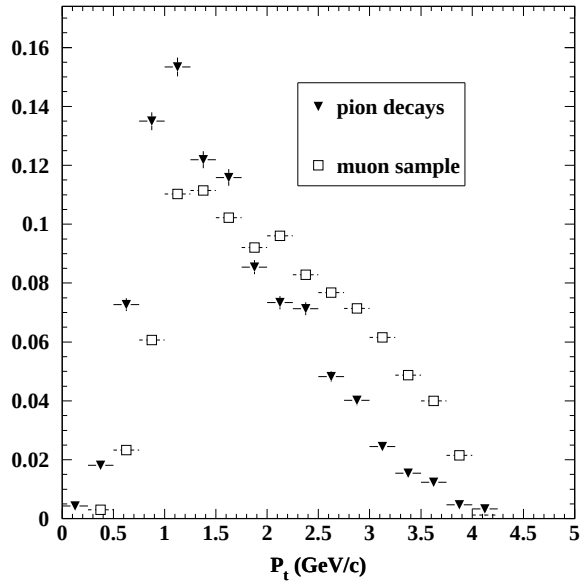

Figure 5.7: The fractional distribution of transverse momenta for both single muons and $\pi^+ \rightarrow \mu^+\nu_\mu$(+ charge conjugate) decays.

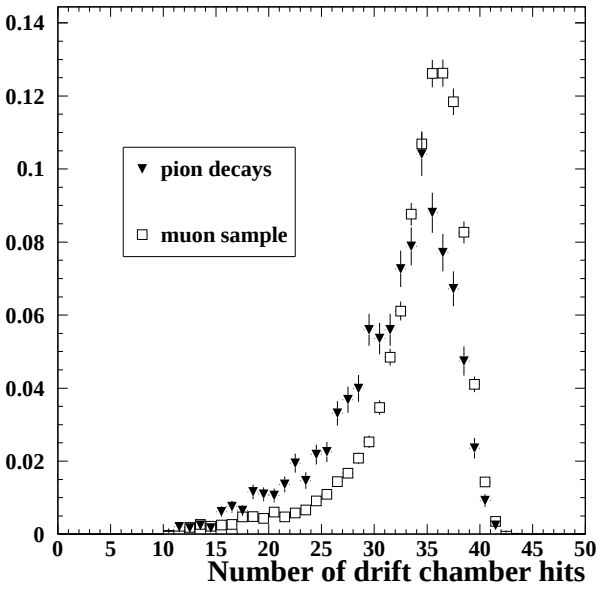

Figure 5.8: The fractional distribution of drift chamber hits for both single muons and $\pi^+ \rightarrow \mu^+\nu_\mu$(+ charge conjugate) decays.

Figure 5.7 shows the generated transverse momentum distribution for single muons and $\pi^+ \rightarrow \mu^+\nu_\mu$(+ charge conjugate) decays. The two distributions are normalised to contain the same number of entries. The decays-in-flight are peaked more towards lower momenta than the single muon tracks are. We show the generated distribution of drift chamber hits for the single muon tracks and tracks from $\pi^+ \rightarrow \mu^+\nu_\mu$(+ charge conjugate) decays in figure 5.8. As with figure 5.7 these distributions are normalised to contain the same number of entries. The majority of tracks in both cases have between 30 and 40 hits in the drift chamber associated with them, however, we see a slightly greater fraction of $\pi^+ \rightarrow \mu^+\nu_\mu$(+ charge conjugate) decays containing less hits than tracks from the single muon sample.

The sample of $\pi^+ \rightarrow \mu^+\nu_\mu$(+ charge conjugate) decays provides a good reference with which to compare the performance of the hypothesis testing variables at distinguishing decays-in-flight from undecayed tracks. We tune cuts to preserve nearly all of the undecayed tracks (to keep high statistics) and determine the fraction of decays rejected. Initial cuts made on the full sample include a cut on $P_t \geq 0.5$ GeV/c (since a major goal of 1-track kink finding is to reduce muon misidentification we focus our attention only on those with sufficient momentum to reach the IFR) and the number of hits ≥ 20 to provide sufficient hits on a track such that the hypothesis testing variables may be applied to it. Looking at figures 5.7 and 5.8 we see that these cuts do not remove a large fraction of our pion decay sample.

We will look at the discrimination available by cutting on each variable individually and then using a combination, with some effort made to obtain the optimal combination. The run test variable will be referred to as Runtest, the correlation sum will be referred to as Corrsum

and the Frühwirth(χ^2) as Früh(χ^2). We will present various combinations to compare these to the χ^2 from the trajectory fit. Table 5.1 shows a summary of the results of this test.

A cut is made on each variable, or combination of variables, to retain 97% of the undeviated track sample. We then apply this cut to the events where there has been a pion decay and find the number that survive. We see that the runtest variable alone doesn't perform as well as the other three which all give similar results, with the Frühwirth(χ^2) providing the best level of discrimination. The most interesting values are found when we start to combine the cuts. We see a slight improvement by combining[2] the P(χ^2) and P(Runtest) over simply using the χ^2 test alone. A subtle difference between the other 'combinations' and this one is that in the following cases we only refer to a combination of cuts being made and no attempt to fuse the variables into a single test statistic is made. The drawback of this is that there is no real assurance that we have an optimal combination of the cuts since we have just tuned the individual cuts to provide us with the desired good track survival fraction. The cut on P(χ^2) was chosen such that it retained 98.5% of the single muon sample and therefore the cuts on the correlation sum and Frühwirth(χ^2) each removed a further 1.5% of the sample. It is interesting to note that by combining each of the three variables with P(χ^2) the rejection efficiencies of the correlation sum and the run test variable are markedly improved whereas that of the Frühwirth(χ^2) actually decreases. The optimal combination of cuts for P(χ^2) and Frühwirth(χ^2) would be to cut on P(χ^2) ≥ 0 and use the cut applied to the Frühwirth(χ^2) alone to preserve 97% of the single muons. This shows a stronger correlation between the Frühwirth and the simple χ^2 from the track fit than is seen when combining P(χ^2) with

[2]The combination of the two is the function X*(1-ln(X)), where X is the product of the two variables; this is what one expects when combining two uncorrelated random variables.

Summary of discrimination from hypothesis testing variables for decays-in-flight from a single pion sample (as described in the text).

variables used	cuts	percentage straight muons surviving	percentage muons from pion decays surviving
Runtest	$\geq$0.228	97.0 $\pm$ 0.2	58.2 $\pm$ 0.9
P(χ^2)	$\geq 2.03 \times 10^{-8}$	97.0 $\pm$ 0.2	30.7 $\pm$ 0.9
Corrsum	$\leq$0.078	97.0 $\pm$ 0.2	35.7 $\pm$ 0.9
Früh(χ^2)	$\leq$50.7	97.0 $\pm$ 0.2	24.8 $\pm$ 0.8
P(χ^2) and P(Runtest)	$\geq 1.25 \times 10^{-7}$	97.0 $\pm$ 0.2	28.0 $\pm$ 0.8
P(χ^2) and Corrsum	$\geq 3.0 \times 10^{-10}$, $\leq$0.128	97.0 $\pm$ 0.2	24.0 $\pm$ 0.8
P(χ^2) and Früh(χ^2)	$\geq 3.0 \times 10^{-10}$, $\leq$53.3	97.0 $\pm$ 0.2	26.1 $\pm$ 0.8
P(χ^2), Früh(χ^2), and Corrsum	$\geq 8.0 \times 10^{-15}$, $\leq$56.0, $\leq$0.14	97.0 $\pm$ 0.2	21.3 $\pm$ 0.8

Table 5.1: The discrimination obtained by making various combinations of cuts on the hypothesis testing variables we have defined is shown here. The 'cut' is the value at which one applies a cut to that corresponding variable to preserve a fixed percentage (97% in this case) of the undeviated muon sample, which we define as the good tracks. We then test what percentage of muons arising from $\pi^+ \rightarrow \mu^+\nu_\mu$(+ charge conjugate) decays in flight survive such a cut. Other cuts made on this sample are described in the text.

Summary of discrimination from hypothesis testing variables for decays-in-flight, taken from a sample of multi-hadron Monte Carlo.

variables used	cuts	percentage straight tracks surviving	percentage muons from pion decays surviving
Runtest	$\geq$0.251	97.0 $\pm$ 0.2	55.8 $\pm$ 7.6
P(χ^2)	$\geq 2.37 \times 10^{-4}$	97.0 $\pm$ 0.2	37.2 $\pm$ 7.4
Corrsum	$\leq$0.058	97.0 $\pm$ 0.2	32.6 $\pm$ 7.2
Früh(χ^2)	$\leq$32.8	97.0 $\pm$ 0.2	32.6 $\pm$ 7.2
P(χ^2) and P(Runtest)	$\geq 5.7 \times 10^{-4}$	97.0 $\pm$ 0.2	34.9 $\pm$ 7.3
P(χ^2) and Corrsum	$\geq 1.2 \times 10^{-6}$, $\leq$0.079	97.0 $\pm$ 0.2	20.9 $\pm$ 6.2
P(χ^2) and Früh(χ^2)	$\geq 1.2 \times 10^{-6}$, $\leq$33.7	97.0 $\pm$ 0.2	32.6 $\pm$ 7.2
P(χ^2), Früh(χ^2), and Corrsum	$\geq 1.0 \times 10^{-8}$, $\leq$39.4, $\leq$0.098	97.0 $\pm$ 0.2	20.9 $\pm$ 6.2

Table 5.2: See description for table 5.1. The the percentage of $\pi^+ \rightarrow \mu^+\nu_\mu$(+ charge conjugate) decays surviving cuts on P(χ^2) has increased making Corrsum a better discriminant in this case. Also, Früh(χ^2) and Corrsum now have the same level of sensitivity to $\pi^+ \rightarrow \mu^+\nu_\mu$(+ charge conjugate) decays.

either the run test variable or the correlation sum variable. In table 5.1 the cuts made in the final entry corresponds to the order in which the variables are written in the table. We see a marked improvement in discrimination when using cuts on three variables, as combined in the final cut selection, over the separate use of each cut.

Table 5.2 shows the same set of cuts applied to a sample of multi-hadron Monte Carlo events. We see a similar level of discrimination and the same trends in the variables

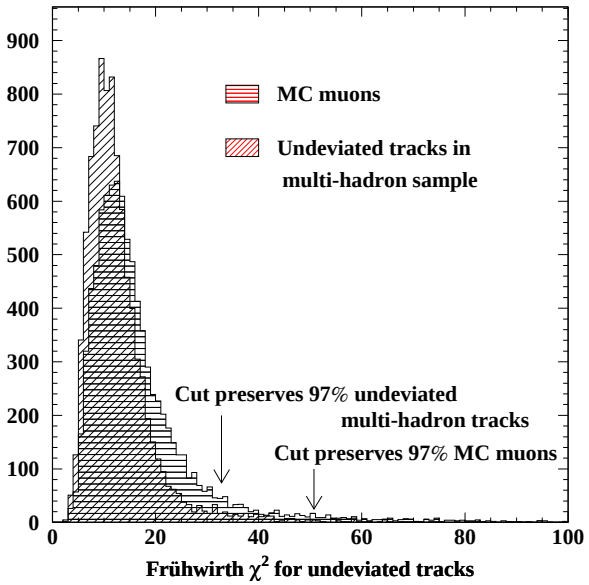

Figure 5.9: A comparison of single muons and undeviated tracks in a multi-hadron sample in the Frühwirth(χ^2) variable.

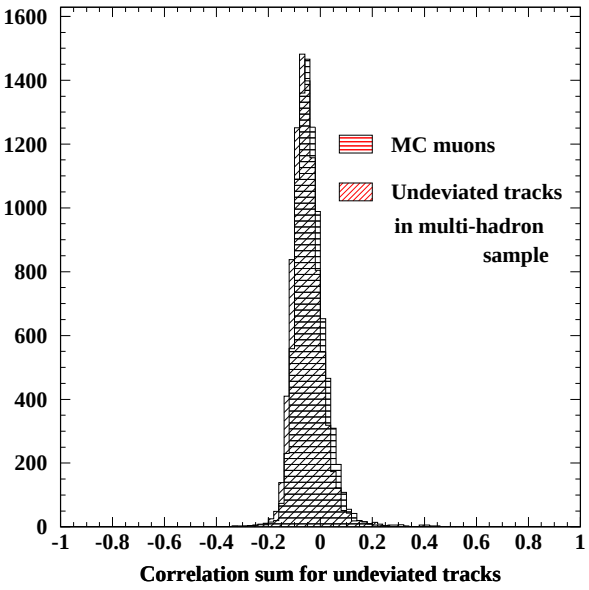

Figure 5.10: A comparison of single muons and undeviated tracks in a multi-hadron sample in the correlation sum variable.

we cut on, such that a combination of cuts gives the best rejection of bad tracks from $\pi^+ \rightarrow \mu^+\nu_\mu$(+ charge conjugate) decays-in-flight. One will notice that between tables 5.1 and 5.2 the cuts made on the hypothesis testing variables to retain 97% of the good tracks have changed markedly. The generation of these two Monte Carlo samples took place in different versions of the BaBar code. Therefore different calibration constants may have been used, and there may not be consistency between the constants in the version used to generate the Monte Carlo and that used to reconstruct the events. In addition, as we show in figure 5.9, the undeviated track samples that are used as the reference on which a 97% cut is tuned are far from identical in the Frühwirth(χ^2) variable. This is also the case for the P(χ^2) distribution and it is the difference in P(χ^2) that probably leads to the difference in Frühwirth(χ^2). In the multi-hadron sample we use all tracks that remain undecayed whereas these are only muons in the generated single muon sample. We show the same distributions for the correlation sum variable in figure 5.10 and see a better match for undeviated tracks from the two samples than that observed in the Frühwirth(χ^2). The sample of Monte Carlo pions that was first used was done so to test the levels of discrimination accessible and one could imagine the set of cuts made on the multi-hadron sample to be a more realistic reflection of what one might expect to see in the real data (this will be examined further in section 5.3). One will notice that the uncertainties have increased in size for the results from the multi-hadron sample compared with the single pions. This is due to reduced statistics for $\pi^+ \rightarrow \mu^+\nu_\mu$(+ charge conjugate) decays existing in the multi-hadron sample as compared to the specifically generated single pion sample.

Figure 5.11 shows the survival fraction for $\pi^+ \rightarrow \mu^+\nu_\mu$(+ charge conjugate) decays in

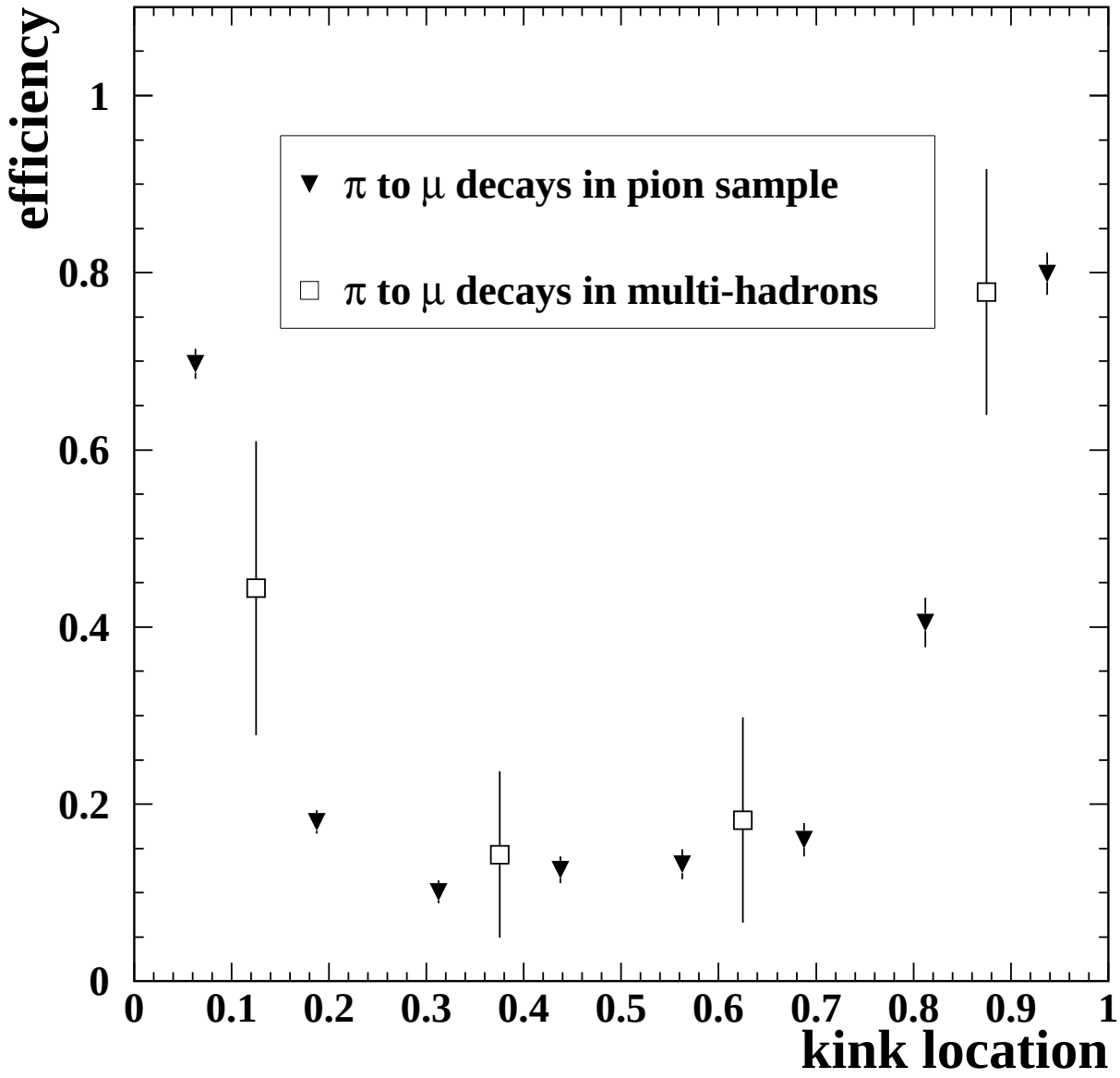

Figure 5.11: The percentage of kinked tracks that survive a cut that preserves 95% of straight tracks as a function of the kink position in the tracking volume.

both the single pion and multi-hadron samples as a function of the position at which the kink occurs. The kink position is given as the position where the kink occurred divided by the total number of hits on the track.

A cut was made on a combination of the Frühwirth(χ^2) and correlation sum such that 95% of the single muon tracks[3] were preserved. This has been done, using only the correlation sum as the hypothesis testing variable, with the simplified Monte Carlo simulation as can be seen in section 5.1 (see figure 5.1 for results). Comparison of figure 5.11 with 5.1 shows that both have similar shapes. We see an improvement in rejection efficiency towards the centre of the tracking volume and a degradation at the edges. However, the simplified Monte Carlo simulation did not include the silicon vertex tracker and contains many assumptions (which are outlined in section 5.1) that were not part of the full BaBar Monte Carlo. We see similar distributions for both the single pion and the multi-hadron samples in 5.11. We note that the error bars on points from $\pi^+ \rightarrow \mu^+\nu_\mu$(+ charge conjugate) decays in the multi-hadron sample are larger than those in the single pion sample due to limited statistics. Upon closer inspection of figures 5.1 and 5.11 we see that the distributions for the full BaBar Monte Carlo are not symmetric about the centre of the tracking volume, whereas those using the simplified Monte Carlo are. Again we note that the distributions in figure 5.11 take advantage of the full SVT-DCH tracking volume whereas the simplified Monte Carlo did not generate any SVT hits. In the simplified Monte Carlo study discrete angular kinks were uniformly distributed throughout the measurement region. However, as

[3]We changed the cut from 97% (as used in tables 5.1 and 5.2) since we wish to compare the rejection as a function of kink position with that in the simplified Monte Carlo simulation, where the cut preserved 95% of the true circular trajectories.

we have already shown in figures 5.7 and 5.8, $\pi^+ \rightarrow \mu^+\nu_\mu$(+ charge conjugate) decays do not have a uniform momentum distribution and are not uniformly distributed throughout the measurement volume in the BaBar Monte Carlo.

Comparing the kinked tracks from the $\pi^+ \rightarrow \mu^+\nu_\mu$(+ charge conjugate) decay sample in the central tracking region, both for the simplified and full BaBar Monte Carlos we see that the survival rate when cutting on both the correlation sum and Frühwirth(χ^2) is improved on that achieved by simply cutting on the correlation sum alone. Since we have already shown the Frühwirth(χ^2) to provide good discrimination in the $\pi^+ \rightarrow \mu^+\nu_\mu$(+ charge conjugate) sample (see table 5.1) this was to be expected.

5.2.1 Using other Methods to Flag Bad Tracks

The aim here is to examine how effective the hypothesis testing variables we have introduced are at finding tracks whose reconstructed parameters differ significantly from their generated parameters. The difference between reconstructed and generated parameters is not possible to calculate in real data. Therefore, seeking a correlation between this difference and the hypothesis testing variables would make us sensitive to flagging these tracks in the data. We take the difference between the fitted and generated Monte Carlo values and using the correlation matrix of errors we can form a χ^2 for 5 degrees of freedom. This will be referred to hereafter as χ^2_{MC}[4]. Large values in the χ^2_{MC} will arise when the fitted parameters are not a good match to the generated values. This may point to some deviation in the track which has not been accounted for, or the possibility that a mistake occurred during the

[4] $\chi^2_{MC} = \Delta^T V^{-1} \Delta$, where $\Delta = (P_f - P_g)$, P_f and P_g correspond to the fitted and generated parameters. V is the covariance matrix of the fitted track.

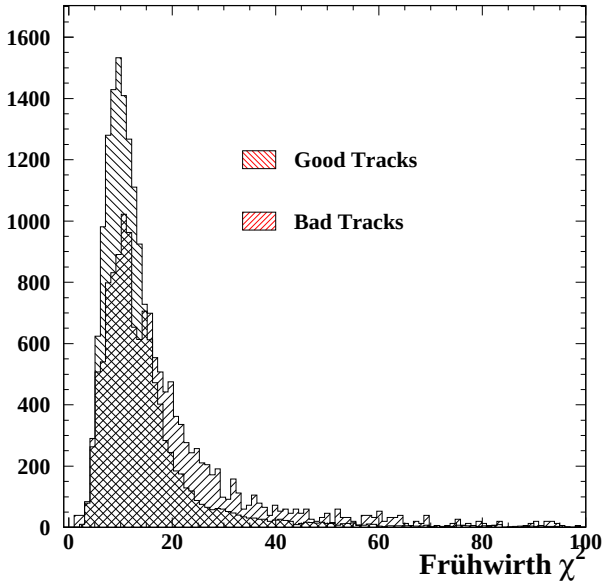

Figure 5.12: The Frühwirth(χ^2) variable for the difference between tracks with a smaller value in $P(\chi^2_{MC})$ and those with a larger value. Description of 'good' and 'bad' tracks can be found in the text.

pattern recognition or the fitting procedure. We compare the values obtained from the fitted trajectory to those generated when the GEANT3 [30] simulation has been run.

Tracks whose fitted parameters are not a good match for their measured parameters will, by definition, exhibit large pulls on their helix parameters. We have also shown that badly reconstructed tracks can be flagged using the test statistics we have introduced. However, it would be instructive to quantify to what extent there are correlations between tracks with large pull values on their helix parameters and a behaviour in one or more of our hypothesis testing variables. For our calculations we transform χ^2_{MC} into a probability distributed between 0 and 1 which we shall call $P(\chi^2_{MC})$.

We begin by defining bad tracks as having $P(\chi^2_{MC}) < 1 \times 10^{-4}$ and good tracks as having $P(\chi^2_{MC}) > 0.1$. We do this since we know that tracks with a large χ^2_{MC} will have a probability

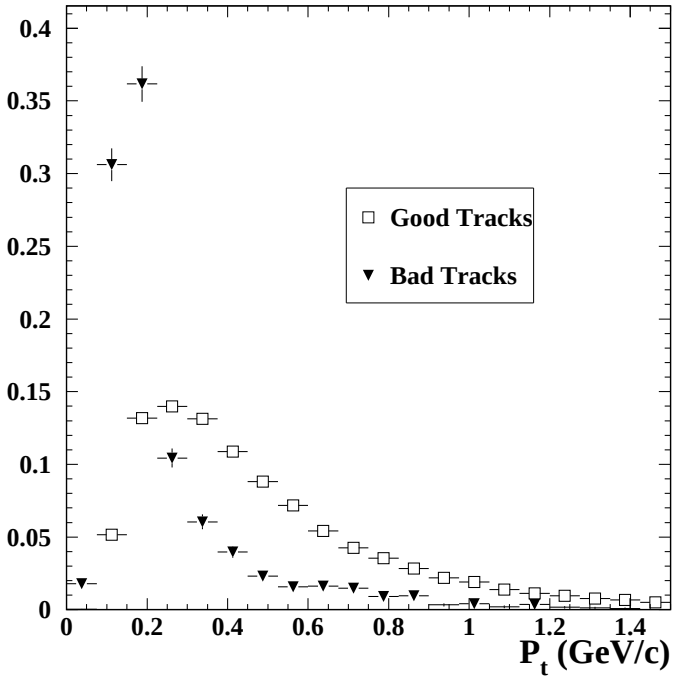

Figure 5.13: The percentage of good and bad tracks that lie in specific ranges of P_t(in GeV/c).

which is peaked towards zero and good tracks should be distributed evenly between zero and 1. Figure 5.12 shows the difference in Frühwirth(χ^2) between those tracks which we have flagged as having good and bad values in P(χ^2_{MC}) (where the two curves have been normalised to contain the same number of events). We can see a region of discrimination between the two curves as the Frühwirth(χ^2) increases. If we tune a combination of cuts on Frühwirth(χ^2) and the correlation sum (as we did in the previous section) to retain $\sim$ 97% of the good track sample, such a cut keeps $86.89 \pm 2.50\%$ of the bad track sample. Therefore, we are not sensitive to removing a large fraction of bad tracks by this method.

Maintaining the same definition of good and bad tracks we examine the momentum dependence of P(χ^2_{MC}). We will use transverse momentum, or P_t, for our comparison since

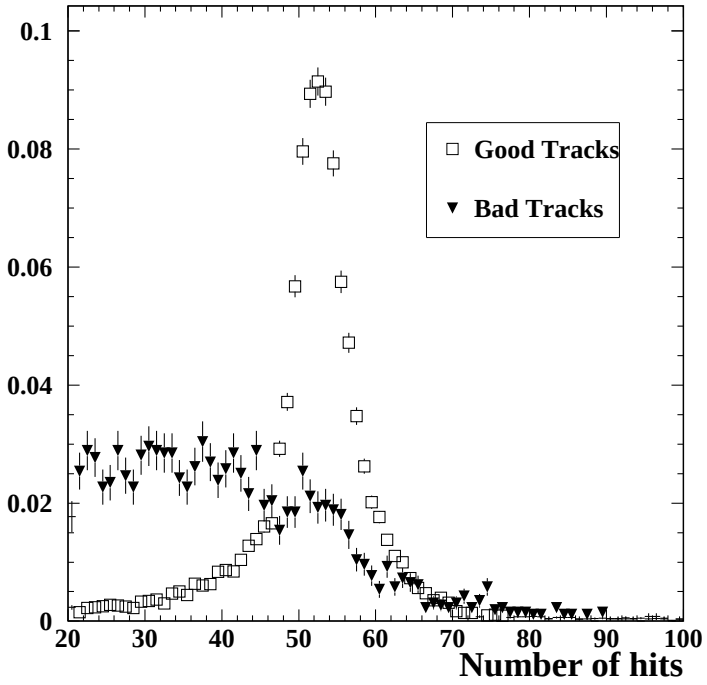

Figure 5.14: The percentage of good and bad tracks that contain a certain number of hits, where hits in both the DCH and SVT are included.

our measuring device is most sensitive in the r-ϕ plane. Figure 5.13 lends itself to looking at this. There is a much higher percentage of bad tracks evident at low momenta than good tracks, with fractions of both tailing off as the momentum increases. We see that approximately 90% of the bad tracks lie in the region with transverse momentum below 0.5 GeV/c.

Figure 5.14 shows the percentage of good and bad tracks that contain a certain number of hits. We see that tracks which have a low $P(\chi^2_{MC})$ generally have a smaller number of hits than those with larger $P(\chi^2_{MC})$ values. There is an increase in the number of good tracks with between 40 and 50 hits, whereas the majority of bad tracks contain less than 50 hits in the tracking volume. One must also note that this plot considers hits left in both the DCH and SVT. Also a cut is made to demand a minimum of 20 hits since any track with less than

Bad Tracks that arise from various sources as a function of P_t.

cut selection	$0<P_t\leq 0.5$	$0.5<P_t\leq 1.0$	$1.0<P_t\leq 1.5$
GTrack(1) = GTrack(n) anomalous hits = 0 pid(1) = pid(n)	61.5±1.1	37.1±3.9	50.0±11.8
GTrack(1) = GTrack(n) anomalous hits > 0 pid(1) = pid(n)	21.6±0.9	27.2±3.6	27.8±10.6
GTrack(1) ≠ GTrack(n) anomalous hits = 0 pid(1) ≠ pid(n)	10.2±0.7	16.6±3.0	5.6±5.4
GTrack(1) ≠ GTrack(n) anomalous hits > 0 pid(1) ≠ pid(n)	6.7±0.6	19.2±3.2	16.7±8.8
Total, number of bad tracks	2064	151	18

Table 5.3: Percentage of tracks with a P(χ^2_{MC}) < 1e-4 broken down into various component processes from which they arose.

this number will not be useful to our study of kink-finding variables.

We can use the output from the simulation, and the parameters obtained when fitting the simulated points, to further categorize good and bad tracks. The output of the GEANT3 simulation are called GHits (short for GEANT hits), each of which comes from an associated GTrack. For a well simulated track one could expect all the GHits to be associated with the same GTrack, however there are instances where this is not the case. We take the generated track, with which we compare the fitted track, to be the one which has the most GHits contributed to it. Hits are generated and smeared by a measurement resolution in the simulation. Track finding and fitting tools are then applied to ultimately form a fitted trajectory which is subsequently entered into the track list. Since we are using information from generated hits to distinguish between kinked and unkinked trajectories we must realise that

Good Tracks broken up into various possibilities as a function of P_t.

cut selection	$0<P_t\leq 0.5$	$0.5<P_t\leq 1.0$	$1.0<P_t\leq 1.5$
GTrack(1) = GTrack(n) anomalous hits = 0 pid(1) = pid(n)	55.1±0.5	60.5±0.7	62.3±1.5
GTrack(1) = GTrack(n) anomalous hits > 0 pid(1) = pid(n)	34.6±0.5	33.0±0.7	33.5±1.4
GTrack(1) ≠ GTrack(n) anomalous hits = 0 pid(1) ≠ pid(n)	5.3±0.2	3.2±0.3	2.1±0.4
GTrack(1) ≠ GTrack(n) anomalous hits > 0 pid(1) ≠ pid(n)	5.0±0.2	3.3±0.3	2.1±0.4
Total, number of good tracks	10181	4703	1087

Table 5.4: Percentage of tracks with a $P(\chi^2_{MC}) > 0.1$ broken down into various component processes from which they arose.

this information is unavailable in real data, where we have no access to the true parameter values.

Tables 5.3 and 5.4 show the detailed composition of tracks in three bins of transverse momentum for good and bad tracks. Again, only those tracks with greater than 20 hits are considered for this study. The cut selection describes those cuts applied to isolate a certain type of track. We note that there is a statistical limitation to any conclusions that can be drawn from the bad tracks with momenta greater than 1 GeV/c since very few events pass this cut. An anomalous hit refers to a hit which has a different GTrack identified with it, when compared to that with which the previous hit and next hit are associated; usually due to noise hits or pattern recognition mistakes. This differs from a change in GTrack in between the first and last hit, as that corresponds to a change over the whole length of the

track where the original GTrack is not returned to. The first two cut selections are what might be considered well defined single tracks, with and without anomalous hits and the final two are what one might suggest are composite tracks. Composite will be used here to refer to those reconstructed tracks that are composed from information from more than one GTrack (tracks with a change in GTrack between their first and last hits). There are marked differences between the two tables. We notice that the percentage of tracks that we would flag as being composite is larger in the sample with large pulls on their helix parameters, which is, a priori, what one might expect. The percentage of well defined single tracks with large pulls on their helix parameters in the bad track sample decreases as we increase the P_t, subsequently the percentage of composite tracks increases. The reverse is true for the good track sample, as the transverse momentum increases the percentage of well defined single tracks increases and that of composite tracks is reduced. However, the conclusion that can be drawn from table 5.3 is that many of the bad tracks have nothing obviously wrong with them.

Having looked at a breakdown of the processes responsible for good and bad tracks as a function of transverse momentum in tables 5.3 and 5.4 we then examined how these may be affected by using the wrong particle type in the fit. This is illuminating since the default particle type that goes into the fit is that of a pion, so differences may arise due to a wrong mass hypothesis being assumed in the fit. We observed that at low momentum, a higher percentage of the composite tracks came from particles not flagged as pions. Also there were less composite tracks at all momenta when the track came from a pion than when the track came from other particle types.

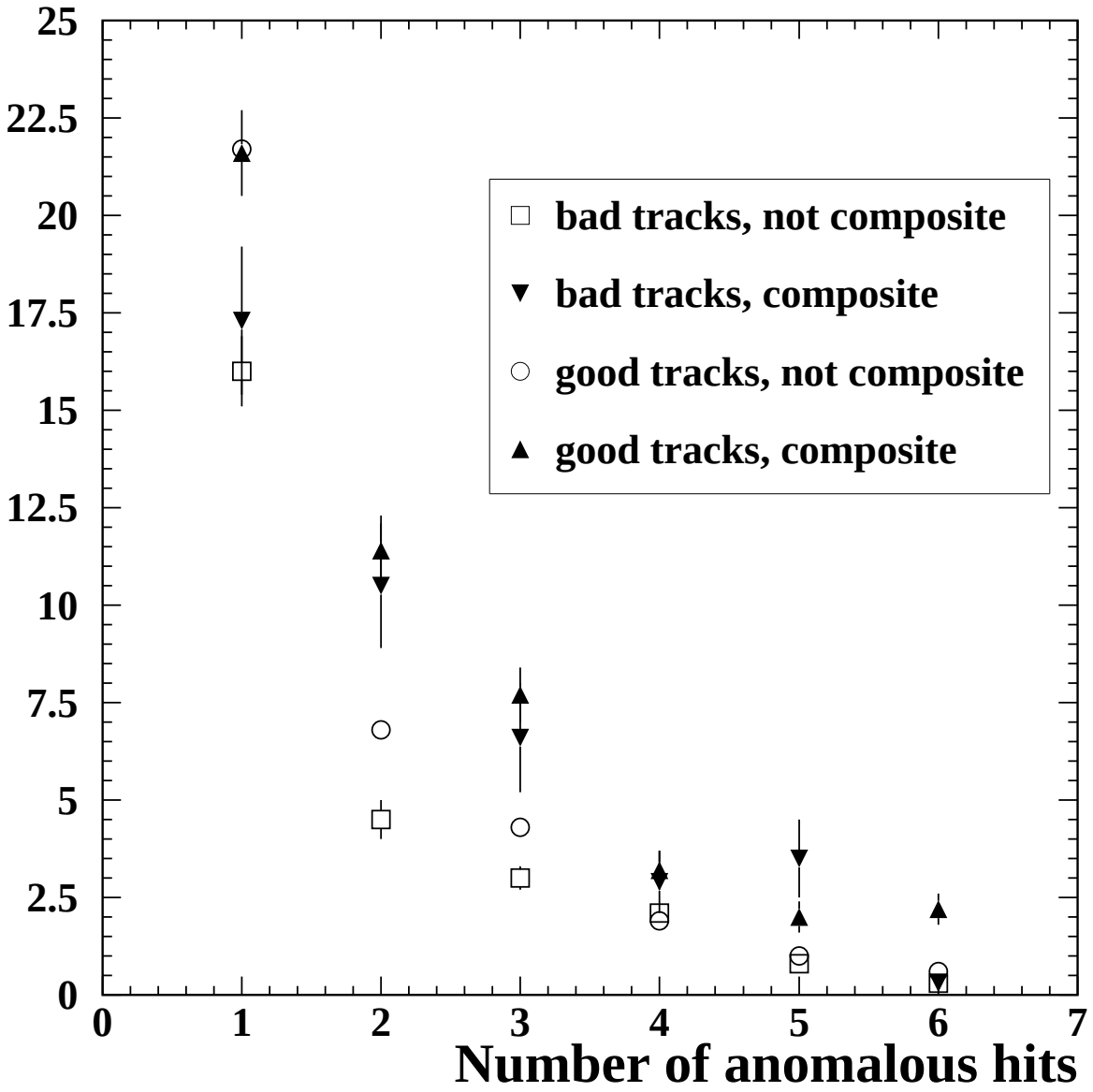

Figure 5.15: The percentage of tracks that contain a certain number of anomalous hits for varying track hypotheses.

We now look at how those tracks that contain anomalous hits vary with differing values of $P(\chi^2_{MC})$ for both composite and non-composite tracks. Figure 5.15 shows the percentage of tracks that contain a certain number of anomalous hits (1 to 6 anomalous hits are considered and all distributions are normalised to the size of the bin with zero anomalous hits). We see for all the four cases plotted the percentage decreases as the number of anomalous hits considered is increased (again a minimum number of hits on a track is 20) and the same shape is evident in all cases. As one would expect, composite tracks that fall into both the good and bad categories, have more anomalous hits than well defined single tracks. We notice that comparing the composite tracks for both cases of good and bad tracks, that the good tracks appear to contain more anomalous hits. This is also the case for trajectories that are not composite. This can be explained by comparing the average number of anomalous hits divided by the average number of total hits for both good and bad tracks. From this we obtain the percentage of hits on a track that are anomalous hits. These values are 2.43% and 2.75% for good and bad tracks respectively. Therefore a larger percentage of the hits on a bad track are anomalous hits than on a good track. So, although figure 5.15 shows that good tracks contain more anomalous hits, we have reasoned that this is due to good tracks being reconstructed from a larger number of hits in the first place. These results show that using the number of anomalous hits on a track does not have a marked effect on the distinction between good and bad tracks.

5.3 Results from the BaBar Data

We wish to look at the extent to which the variables we have been testing are useful on real data.

Figures 5.16 and 5.17 show the discrimination between tracks from dimuon events and multi-hadron events in real data using the correlation sum and Frühwirth(χ^2) respectively. Again these plots have the same cuts on $P_t(\geq 0.5$ GeV/c) and the number of hits(≥ 20) that were used in the previous studies. One should note that the dimuon and multi-hadron samples have been rescaled to contain the same number of events as the single muon Monte Carlo, which is also plotted. We wish to test two things with these plots, 1) are the Monte Carlo muons a good match for the muons in real data and, 2) do we see a difference in the real data between multi-hadrons and muons. In figure 5.16 there are only slight differences between the three distributions. This is good for the comparison of muons in data and Monte Carlo since it shows that they are well matched in the correlation sum variable. However, in figure 5.17 one can notice a marked difference in all three distributions. The generated muons in the Frühwirth(χ^2) variable do not match well with the muons from the real data. The region of interest for the comparison of data from muons and multi-hadrons in both variables is in the small tail at positive x. Hence this is the region one must focus on to look for discrepancies between the real data samples.

To emphasize these tails a cut is applied to preserve 3% of the real muon distributions in both figure 5.16 and figure 5.17. The number of multi-hadron events which survive the cut is then noted and the two can be compared. After normalisation, 91.4 real muon tracks

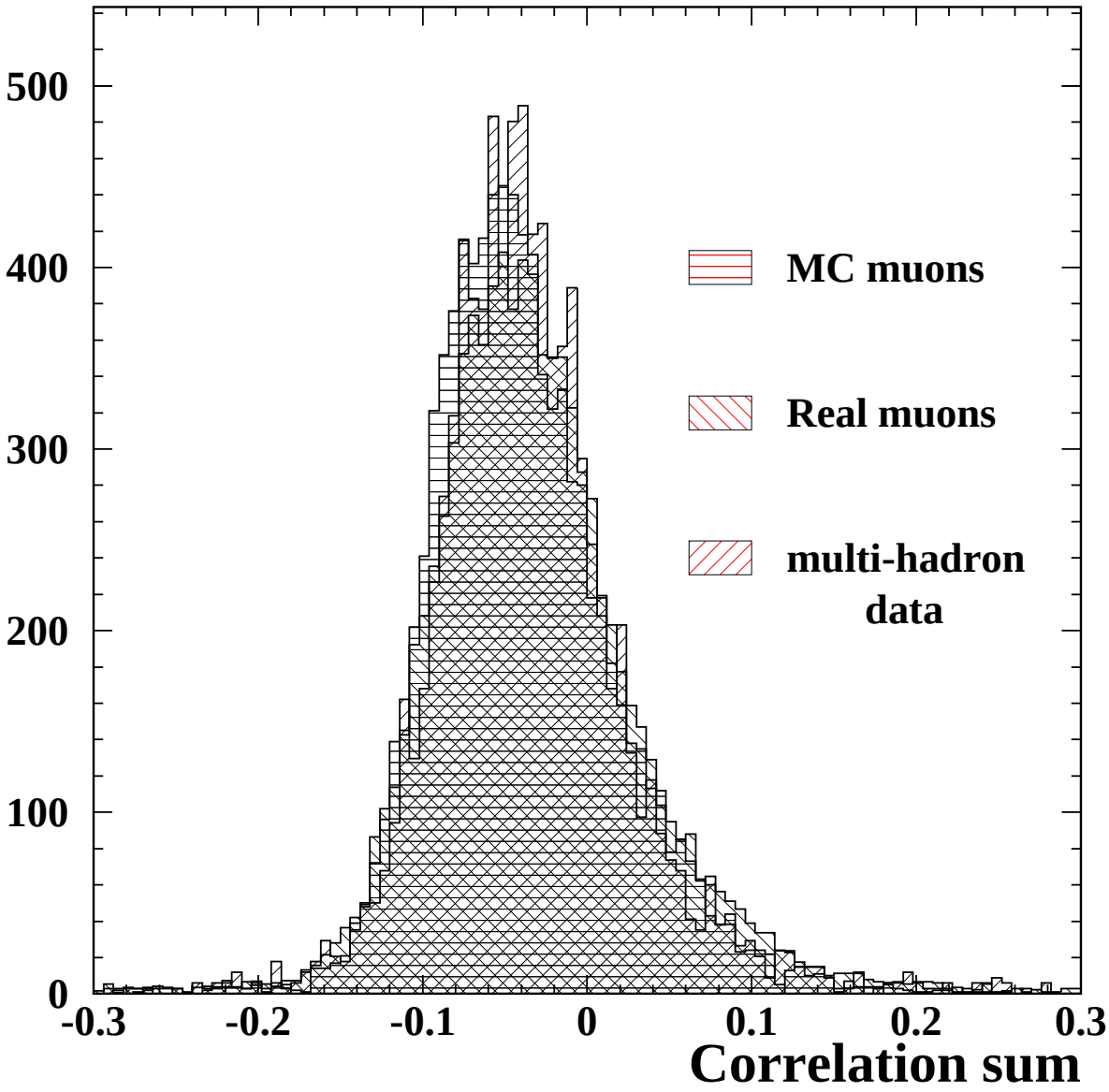

Figure 5.16: The correlation sum for real data from BaBar. We show a skim of dimuon events and a collection of multi-hadrons, the Monte Carlo muon distribution is overlayed for comparison.

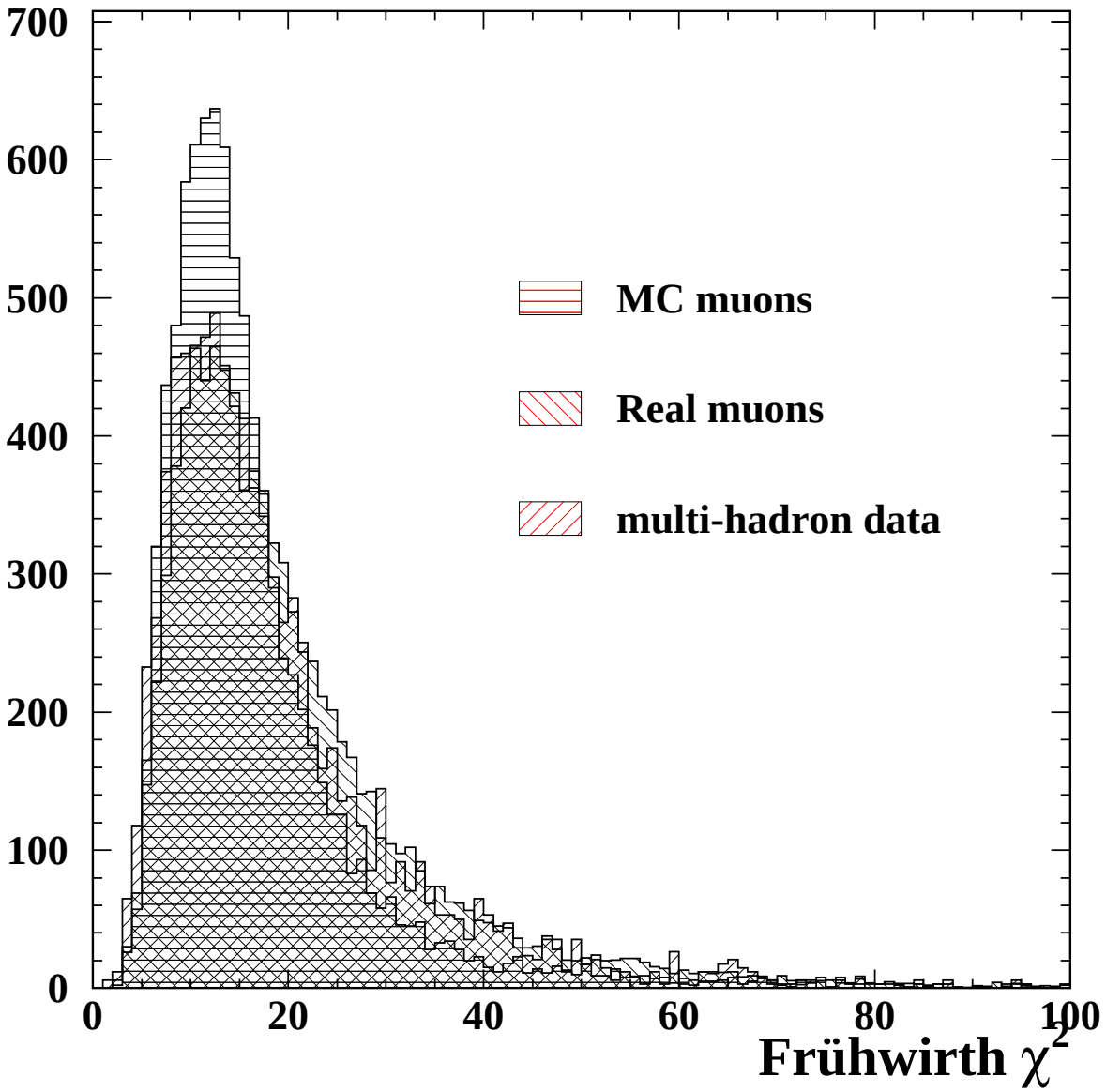

Figure 5.17: The maximum value of Frühwirth(χ^2) for real data from BaBar. We show a skim of dimuon events and a collection of multi-hadrons, the Monte Carlo muon distribution is overlayed for comparison.

remained, corresponding to 3% of the distribution. The cut on real multi-hadron data in the correlation sum yielded 82 tracks and in Frühwirth(χ^2) yielded 85 tracks. When the number of real muons is subtracted from the number of multi-hadrons one obtains,

$$\text{Correlation sum} = -9.4 \pm 10.1$$

$$\text{Frühwirth}(\chi^2) = -6.4 \pm 10.2.$$

Using the multi-hadron Monte Carlo simulation a calculation was performed to estimate the number of $\pi^+ \rightarrow \mu^+\nu_\mu$(+ charge conjugate) decays we might expect to see in the real data. We observed 27 $\pi^+ \rightarrow \mu^+\nu_\mu$(+ charge conjugate) decays out of 61 kinked tracks (where a kinked track is any composite track) applying a cut to the Correlation sum, and 25 $\pi^+ \rightarrow \mu^+\nu_\mu$(+ charge conjugate) decays out of 48 composite tracks in the Frühwirth(χ^2) variable. Normalising these values to the total number of real multi-hadron events one would expect the total number of kinked tracks in each variable to be,

$$\text{Correlation sum} = 30 \pm 3.8$$

$$\text{Frühwirth}(\chi^2) = 24 \pm 3.4.$$

Therefore, the number of expected kinks is inconsistent with the number observed.

One difference between the muon and multi-hadron tracks from real data is in the momentum distributions, since the muons will have a larger average momentum than the multi-hadrons. The average amount of multiple scattering on a lower momentum track will be greater than that on a track of higher momentum. Therefore, if there is an error due to mis-alignment for example, this will be more noticeable in the sample of higher momentum tracks than in the lower momentum tracks. If the amount of scattering included in the fit

is reduced then the effect due to an alignment error will be more pronounced than if many significant scatters were included. The muon data will produce a larger average number of hits per track than multi-hadron data. Therefore the maximum value of Frühwirth(χ^2) will be larger, since if there are a greater number of hits on the track there is a greater probability of one giving a large mis-match χ^2. These effects may be possible causes for the disparity between kinked tracks in the multi-hadron data and muon data.

Chapter 6

Conclusions

We have presented here a study of 1-track kink-finding using a set of hypothesis testing variables compared with, and combined with, the standard χ^2 from the track-fit. We demonstrate an ability to improve the rejection efficiency of badly fitted trajectories, from a sample containing both kinked and unkinked tracks. This was done by using both the variables we have created (the run test variable and the correlation sum [27]), and those defined by others (the Frühwirth(χ^2) [28]), along with the simple track-fit χ^2.

The discrimination between kinked and unkinked tracks achieved with these variables was examined, not only in Monte Carlo simulations, but also in real data from the BaBar experiment. Much of the focus of this study was on $\pi^+ \rightarrow \mu^+\nu_\mu$(+ charge conjugate) decays-in-flight. Muon identification is important in measuring semi-leptonic B decays which are used to tag B flavour. Hence any mis-identification resulting from $\pi^+ \rightarrow \mu^+\nu_\mu$(+ charge conjugate) decays would impact this measurement. We have examined $\pi^+ \rightarrow \mu^+\nu_\mu$(+ charge conjugate) decays in both single pion and multi-hadron Monte Carlo. We studied correlations between kinked tracks and the number of hits left by a particle, its transverse momentum and the position of the deviation within the measurement volume. Through our tests on

Monte Carlo simulations, we have also shown the ability to reject kinked tracks from various other sources by looking at changes in the generated track associated with each hit and the number of anomalous hits on a track. We have also established that the hypothesis testing variables investigated do not provide good discrimination between those tracks that have a good match between their generated and reconstructed parameters, and those that do not. Results have also been obtained using real data from BaBar applying the kink-finding variables we have discussed. No variation was seen between the muon and multi-hadron samples in the data.

These hypothesis testing variables, given their ease of calculation, may be applied to a wide range of cases where an error may have occurred during the fitting of a trajectory. The run test and correlation sum are implemented as part of the BaBar code, along with the Frühwirth(χ^2). All three of these variables are made available to users to assist in their analyses.

Bibliography

[1] Glashow, S. L., Illiopoulos, J., and Maiani, L., Phys. Rev. Lett. **D 2** (1970) 1285.

[2] Weinberg, S., *A Model of Leptons*, Phys. Rev. Lett. **19** (1967) 1264.

[3] Salam, A., *Elementary Particle Theory*, Ed. N. Svartholm, (Almquist and Wiksells, Stockholm, 1969) 357.

[4] Kobayashi, M., and Maskawa, T., *CP Violation in the Renormalizable Theory of Weak Interaction*, Prog. Theor. Phys. **49**, 652 (1973).

[5] Groom, D., et al, *Review of Particle Physics. Particle Data Group*, The European Physical Journal. C15, 1 (2000).

[6] Wolfenstein, L., Phys. Rev. Lett. **51**, 1945 (1983).

[7] Cabibbo, N., Phys. Rev. Lett. **10**, 531 (1963).

[8] Richman, J. D., *Heavy Quark Physics and CP Violation*, (Elsevier Science B. V., 1998).

[9] Harrison, P. F., and Quinn, H. R., [BaBar Collaboration], *The BaBar Physics book : Physics at an asymmetric B factory*, (1998).

[10] Christenson, J. H., Cronin, J. W., Fitch, V. L. and Turlay, R., *Evidence for the 2π decay of the K_0^2 Meson*, Phys. Rev. Lett. **13**, 138 (1964).

[11] Sakharov, A., D., *Violation of CP Invariance, C Asymmetry and Baryon Asymmetry of the Universe*, Pisma Zh. Eksp. Teor. Fiz. 5, 32 (1967).

[12] Forti, F., *TRACKERR studies for optimization of vertex detector resolution*, **SLAC-BABAR-NOTE-195**.

[13] Bozzi, C., et al. *The BaBar Silicon Vertex Tracker* Nucl. Instrum. Meth. **A435** 25-33 (1999).

[14] Sciolla, G., et al *The BaBar Drift Chamber*, Nucl. Instrum. Meth. **A419** 310 (1998).

[15] Boyarski, A., Briggs, D., Burchat, P., *Studies of helium based drift chamber gases for high luminosity low energy machines*, Nucl. Instrum. Meth. **A323** 267 (1992).

[16] Mancinelli, Giampiero, Private Communication.

[17] Schwiening, Jochen, Private Communication.

[18] Boutigny, D., et al [BaBar Collaboration], *BaBar Technical Design Report*, **SLAC-R-0457**.

[19] Panetta, Jim, Private Communication.

[20] Billoir, P., *Nucl. Instrum. Meth.* **A255** (1984) 352.

[21] Frühwirth, R., *Nucl. Instrum. Meth.* **A262** (1987) 444.

[22] Meyer, S. L., *Data Analysis for Scientists and Engineers*, Wiley, New York (1975).

[23] Kendall, M. G., Stuart, A., *The Advanced Theory of Statistics in three volumes*, Griffin, London (1963-1968)

[24] Brown, D. N., *An object-oriented extended Kalman filter tracking algorithm*, Talk given at Computing in High-Energy Physics (CHEP 97), Berlin, Germany 7-11 Apr (1997).

[25] Brown, D. N., Charles, E. A., Roberts, D. A., *The BaBar Track Fitting Algorithm*, Talk given at Computing in High-Energy Physics (CHEP 2000), Berkeley, Feb (2000).

[26] Albert, J., *BaBar Kinkfinding Software*, BaBar Analysis Document #31.

[27] Kowalewski, R. V., Jackson, P. D., *Track Fit Hypothesis Testing and Kink Selection using Sequential Correlations*, Accepted for publication in *Nucl. Instrum. Meth.* e-print archive, **hep-ex/0004008**.

[28] Frühwirth, R., *Application of filter Methods to the Reconstruction of Tracks and Vertices in events in Experimental High-Energy Physics*, **HEPHY-PUB 516/88** (Vienna, Dec. 1988)

[29] Astier, P., et al. *Kalman Filter Track Fits and Track Breakpoint Analysis*, *Nucl. Instrum. Meth.* e-Print Archive, **physics/9912034**.

[30] More information about the GEANT3 simulation can be found here :

http://wwwinfo.cern.ch/asdoc/geant_html3/geantall.html

Appendix A

Hypothesis Testing and Kink Selection using Sequential Correlations

A.1 Introduction

Trajectory fitting aims to determine a set of fitted parameters and to test the validity of the trajectory hypothesis. Both of these questions are usually addressed by minimizing a χ^2 constructed from the squares of the deviations between the measurements and the parameterized trajectory. Known sources of correlation can be incorporated into the definition of the χ^2. The value of χ^2 at the minimum is used to test the adequacy of the fitted hypothesis. [5,22,23] However, additional (unforeseen) correlations arise naturally in trajectory fitting, where adjacent measurements are in causal order. Deviations from the expected trajectory due to either a discrete change at some point (e.g. a scattering or decay in flight) or to a continuous parameter change (e.g. dE/dx energy loss or magnetic field anomalies) introduce correlated shifts in the positions of all subsequent measurements. The χ^2 test is not very sensitive to these trajectory deviations when they are small on the scale of the

measurement errors, since it considers only the squares of the residuals.[1]

This paper introduces new quantities for hypothesis testing that are applicable to any fits for which an ordering variable (e.g. time) can be identified.[2] The mean correlation of ordered sets of residuals (nearest neighbor, next nearest neighbor, etc.) are used for this purpose. These correlations are essentially independent of χ^2, and test the assumption that the measurements are mutually independent (or, more generally, that the correlations amongst the measurements are properly accounted for in the fit). It should be noted that the presumption of the independence of the measurements once known sources of correlation (e.g. multiple Coulomb scattering) are taken into account is also present in sequential fitting methods such as the Kalman Filter [20, 21], and the correlation test developed here can be applied to the output of such a fit.

The power of these correlation statistics for hypothesis testing is studied as a function of several trajectory deviations that arise naturally in charged particle tracking. For simplicity, the trajectories studied are circular arcs, corresponding to the projection of charged particle trajectories onto a plane transverse to a uniform axial magnetic field. The following sections describe the correlation variables, the simulation used to measure their effectiveness, and the improvement in discrimination between true and false hypotheses beyond what can be achieved using χ^2 alone.

[1] The term residual in this paper refers to the signed distance of closest approach between a measurement and the fitted trajectory divided by the uncertainty assigned to the measurement.

[2] Not all fits are in this category: e.g. one cannot in general define a useful ordering variable for vertex fits.

A.2 Description of correlation variables

The degree to which nearby measurements are correlated can be gauged by considering the mean correlation as a function of the distance between measurements. Using the standard correlation estimator [22] to form an average correlation

$$r_k = \sum_{i=1}^{N-k} \frac{\delta_i \, \delta_{i+k}}{\sigma_i \, \sigma_{i+k}} \; / \; \sqrt{\left(\sum_{i=1}^{N-k} \frac{\delta_i^2}{\sigma_i^2} \right) \left(\sum_{i=1}^{N-k} \frac{\delta_{i+k}^2}{\sigma_{i+k}^2} \right)} \tag{A.1}$$

as a function of the distance between measurements gives fairly good discrimination between true and false trajectory hypotheses. The sums run from 1 to $N - k$, N is the number of measurements on the trajectory, δ_i is the signed distance to the fitted trajectory for measurement i, σ_i is the estimated uncertainty of measurement i, and k is the correlation distance: $k \in [1, N-1]$. However, the following combination,

$$\rho_k = \sum_{i=1}^{N-k} w_{ik} \frac{2 \, \delta_i \, \delta_{i+k}}{\delta_i^2 + \delta_{i+k}^2} \; / \; \sum_{i=1}^{N-k} w_{ik} \;\; ; \;\; w_{ik} = \frac{\delta_i^2 + \delta_{i+k}^2}{\sigma_i^2 + \sigma_{i+k}^2} \tag{A.2}$$

motivated by considering the measure $(\delta_i - \delta_{i+k})^2 \, / \, (\sigma_i^2 + \sigma_{i+k}^2)$, gives slightly better discrimination.[3] This is because the correlation sought is in the actual distances δ from the fitted trajectory, not in the residuals δ/σ. The weight factor emphasizes those pairs of measurements with significant deviations. These correlation measures satisfy $|\rho_k| \leq 1$ for all k. For uncorrelated measurements the expectation values of the ρ_k are close to zero. Negative correlations are introduced by the trajectory fit; they are small provided the number of fitted parameters is much smaller than the number of measurements.

[3] This formulation is appropriate for use in cases where known sources of correlation (e.g. multiple Coulomb scattering) are incorporated using a sequential fitting method, in which case the residuals at each measurement can be taken as independent.

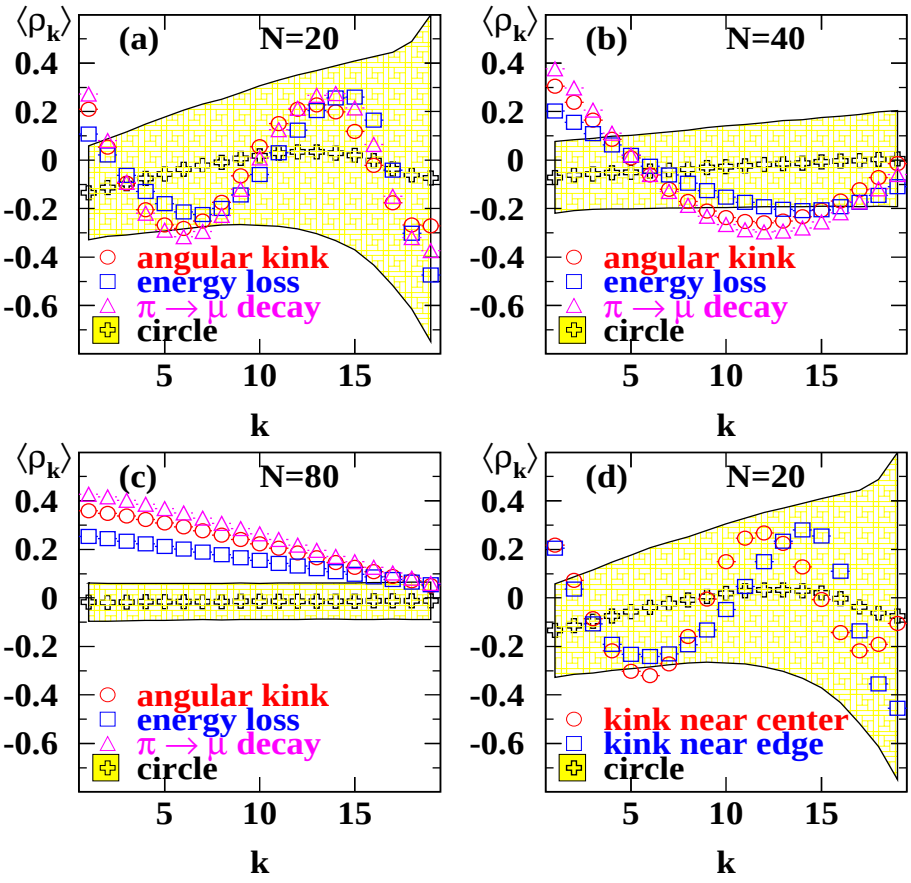

Figure A.1: The expectation value of the correlation variable ρ_k is shown as a function of the correlation length k. The first 19 $\langle \rho_k \rangle$ are shown for 20 (a), 40 (b) and 80 (c) measurements. The different symbols correspond to specific generated trajectories; the fitted trajectory is a circle in each case. The shaded region indicates the r.m.s. of the ρ_k distribution for the circle trajectory. (d) shows $\langle \rho_k \rangle$ for angular kinks occurring at different locations.

Fig. A.1(a-c) shows the expectation value[4] of each ρ_k as a function of the correlation distance k (for k up to 19) for true circle trajectories and for three common trajectory deviations: a discrete angular kink, an uncorrected continuous energy loss and the decay in flight of a pion to a muon. The locations of the angular kink and decay in flight were uniformly distributed along the trajectory. The fitted trajectory in each case was a circular arc. The magnitudes of the $\langle\rho_k\rangle$ for the incorrect hypotheses depend on the particular choice of parameters in the simulation. The number and location of the crossing points between $\langle\rho_k\rangle$ for the incorrect trajectory hypotheses and $\langle\rho_k\rangle$ for the correct hypothesis are very similar for the trajectory deviations studied here. Fig. A.1(d) compares a sample with a discrete angular kink located near the center of the measurement region with a sample where the kink is located closer to the edge of the measurement region. The kink location clearly has an impact on the behavior of $\langle\rho_k\rangle$, most notably for large k/N.

Using all of the ρ_k values gives the best discrimination between the correct hypothesis and a particular type of incorrect hypothesis, but does not provide optimal discrimination for all types of incorrect hypothesis as can be seen by considering the different shapes (note in particular the locations of the extrema) of the trajectory hypotheses shown in Fig. A.1. Furthermore, most of the discrimination power is concentrated at small k, since the r.m.s. of the ρ_k distributions expected for the correct hypothesis are smallest there.[5] These considerations, along with the essentially linear behavior of the difference $\langle\rho_k\rangle_{\text{false}} - \langle\rho_k\rangle_{\text{true}}$ as

[4] Calculated numerically using the simulation described below.

[5] The number of correlation measures summed for a given k is $N - k$, giving a statistical error proportional to $1/\sqrt{N-k}$.

a function of the correlation distance k for small k/N, lead us to the following test statistic:

$$\lambda = \sum_{k=1}^{L} C_k \rho_k \text{ with } C_k = \frac{2}{L(L-1)}(L-k) \text{ and } \sum_{k=1}^{L} C_k = 1. \quad (A.3)$$

Choosing L as the nearest integer to N/8 was found to give good sensitivity to the trajectory deviations studied.

A.3 Description of simulation

The sensitivity of λ to trajectory deviations was studied using a simple simulation. Charged particles were generated and tracked through a uniform axial magnetic field and measured points were generated in the plane orthogonal to the magnetic field direction. The measurement uncertainty was taken as Gaussian. Trajectories were generated with parameters typical of charged particle tracking detectors [18]:

- average hit resolution: 150 μm;
- variation in resolution: factor of 5 between the best and worst measured points;
- radial difference between first and last measurement layer: 54 cm;
- number of measurements: varied from 20 to 160;
- magnetic field: axial field of magnitude 1.5 Tesla;
- initial particle momentum between 0.5 GeV/c and 5 GeV/c.

The measurements were uniformly distributed along the trajectories, the hit efficiency was unity and no noise hits were generated. The location of discrete trajectory deviations (angular kink or particle decay) was randomly distributed along the trajectory. The generated

points were fitted to a circle assuming perfect pattern recognition, i.e. all generated measurements were used in the fit.

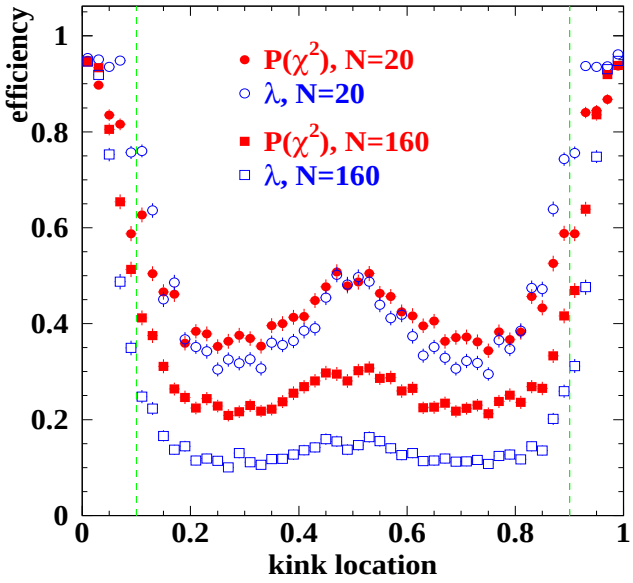

Figure A.2: The survival rate as a function of the location of a discrete angular kink within the measurement volume. The cuts on λ and $P(\chi^2)$ are set to give 95% efficiency for true circular trajectories. The dashed lines bound the region used for subsequent study of the power of each variable.

A.4 Results

The generated data were used to study the discrimination power of λ and of χ^2 as a function of specific trajectory deviations. Fig. A.2 shows the fraction of trajectories surviving a cut on λ or on the χ^2 probability $P(\chi^2)$ as a function of the position of a discrete angular kink, where the kink angle was uniformly distributed between ± 0.02 radians. The cuts were set to give 95% efficiency for true circular trajectories. There is little discrimination power for kinks occurring at either end of the measurement region. Based on this, only those trajectory deviations occurring within a fiducial region consisting of the central 80% of the

measurements were selected for subsequent study.

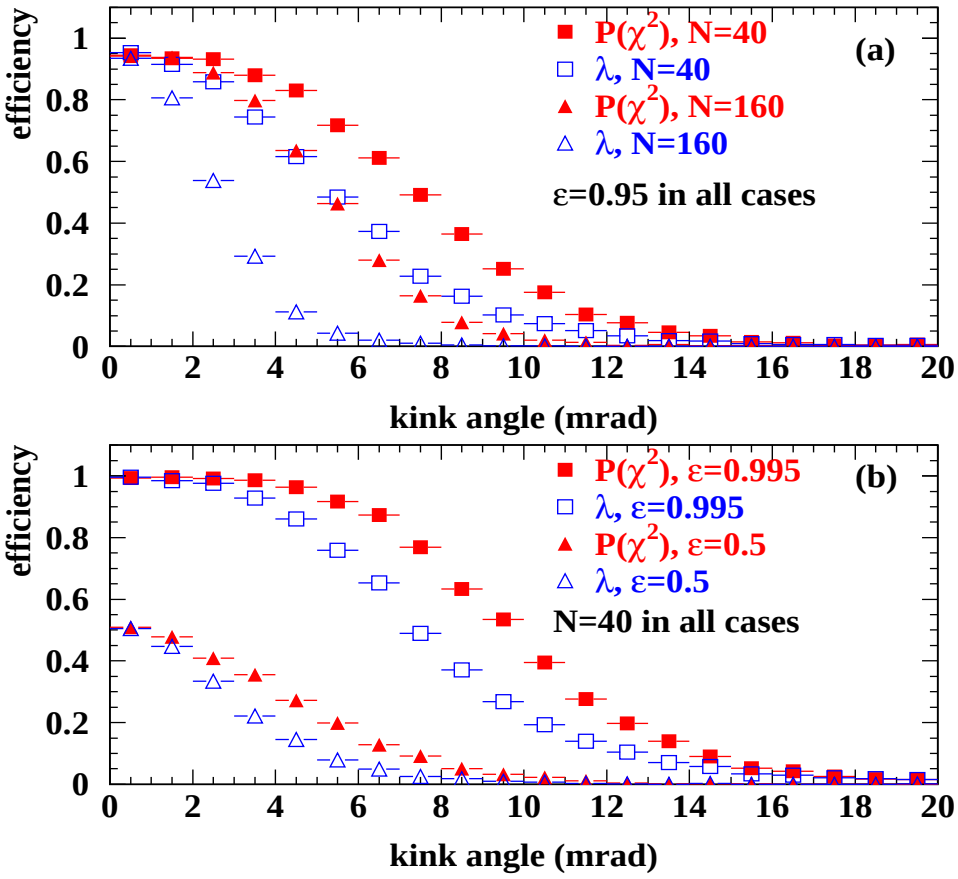

Figure A.3: The survival rate as a function of the size of a discrete angular kink within the fiducial region. The behavior for different N is shown in (a) for a cut that gives an efficiency ϵ of 95% for true circular trajectories. The curves in (b) show the effect of varying the cut on ϵ.

The fraction of these selected trajectories surviving a cut that gives 95% efficiency for true circular trajectories is shown as a function of the size of the angular deviation in Fig. A.3. The correlation variable λ is more powerful than P(χ^2) provided N > 20 and becomes relatively more powerful as the number of measurements increases. This is to be expected, since the physical correlation length sampled by λ is of the order of $\frac{1}{8}$ of the track length, and increasing

the density of measurements allows a more precise determination of the correlation. Similar behavior is observed for different choices for the efficiency for true circular trajectories. The power of λ and $P(\chi^2)$ to discriminate $\pi \rightarrow \mu$ decays from true circular trajectories is shown in Fig. A.4. Note that the decay angle between the π and μ does not in general lie in the

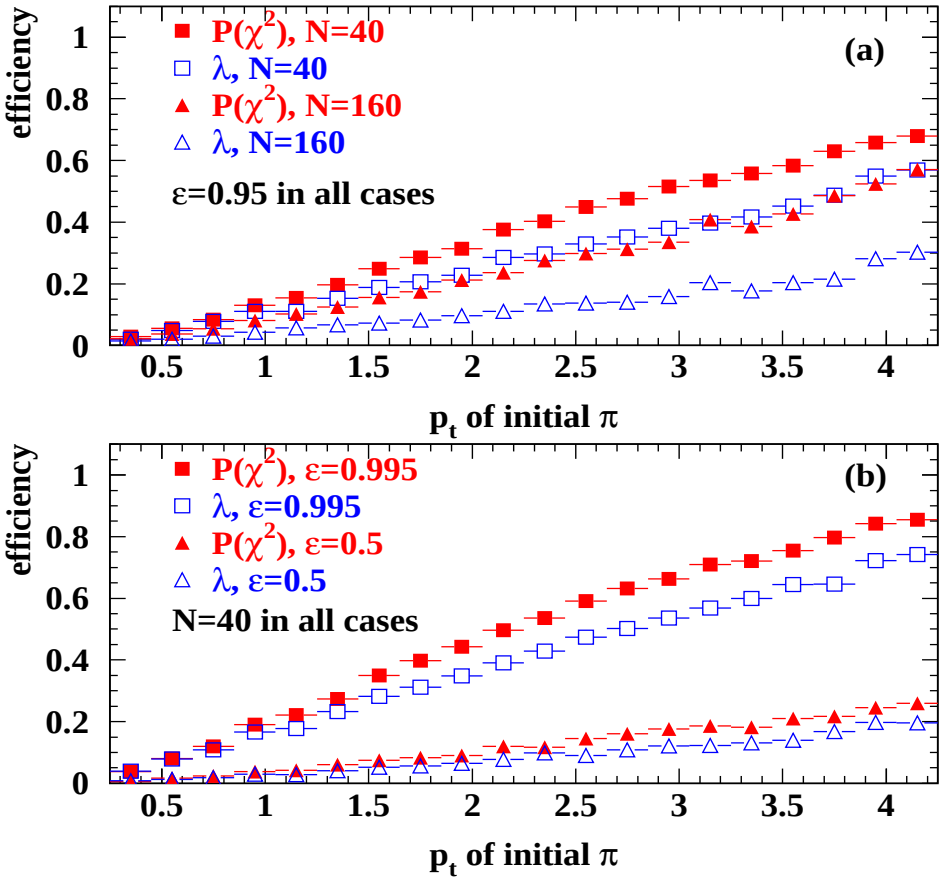

Figure A.4: The survival rate for $\pi \rightarrow \mu$ decays occurring in the fiducial region as a function of the initial momentum of the pion in the plane transverse to the magnetic field. The behavior for different N is shown in (a) for a cut that gives an efficiency ϵ of 95% for true circular trajectories. The curves in (b) show the effect of varying the cut on ϵ.

measurement plane, and that the momentum of the muon will be smaller than that of the pion. The correlation variable λ is again a significantly better discriminant than is $P(\chi^2)$.

The extent to which the discrimination afforded by λ is optimal was studied. The measurements along trajectories generated with a discrete angular kink were fitted using both the correct hypothesis, i.e. two circular arcs of constant curvature with an angular deviation at a point, and using the nominal (incorrect) hypothesis of a single circular arc. The ratio of the resulting χ^2 probabilities $P_{\rm circle}(\chi^2)/P_{\rm correct}(\chi^2)$ is an optimal discriminant variable in this case.[6] The position of the angular kink was taken as either the true position of the generated deviation (denoted "fixed $R_{\rm kink}$" in Fig. A.5) or as the best fit value after considering all potential kink positions (denoted "fitted $R_{\rm kink}$" in Fig. A.5). The kink position will in general be unknown, so the "fitted $R_{\rm kink}$" curve is in practice the best one can achieve. As is seen in Fig. A.5, the correlation variable λ gives discrimination that approaches the optimal value as the number of measurements increases.

A.5 Discussion

The correlation variables $\rho_{\rm k}$ introduced here test the assumption that a set of measurements are mutually independent once known sources of correlation have been taken into account. Use of the simple combination of $\rho_{\rm k}$ introduced here as λ leads to an improvement in the sensitivity for detecting small trajectory deviations relative to that achievable using $P(\chi^2)$. This additional goodness-of-fit test is independent of the χ^2 test, and can be applied to the residuals from both traditional least squares fits and from Kalman filter fits. The improved sensitivity to small deviations can be qualitatively understood by recognizing that χ^2 has a quadratic dependence on individual deviations, while λ has a linear dependence. For

[6] In practice, trajectory deviations of several different types may be present in a sample, so fitting for one particular type of deviation will not be optimal.

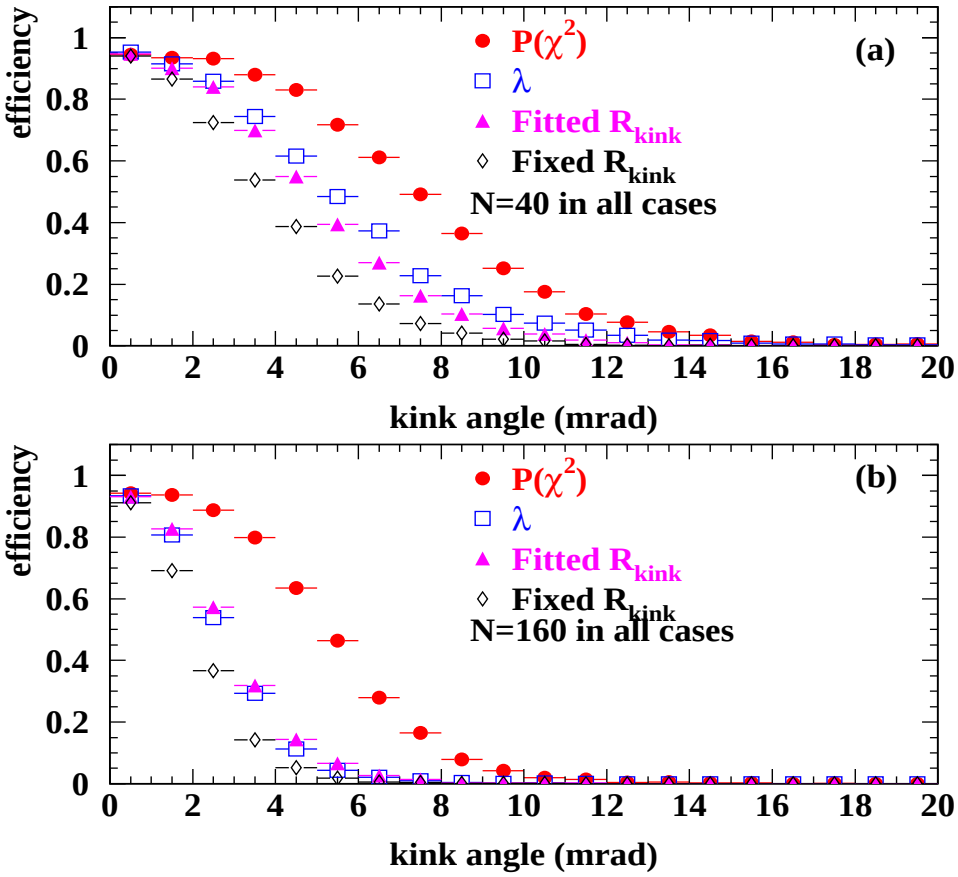

Figure A.5: The survival rate as a function of the size of a discrete angular kink for 40 (a) and 160 (b) measurements. The cuts on λ and $P(\chi^2)$ are set to give 95% efficiency for true circular trajectories. Also shown are results from an optimal technique (see text) with the kink location either fixed to the generated position ("fixed R_{kink}") or determined by the fit ("fitted R_{kink}").

larger deviations (not shown here) $P(\chi^2)$ becomes a more powerful discriminant than λ, as expected. For the deviations studied, the gain from combining the λ and $P(\chi^2)$ tests was negligible.

The λ and χ^2 tests have different dependencies on the input to the fit. The χ^2 test is sensitive to the scale of the assigned measurement errors σ_i and can be compromised by mis-estimates of and non-Gaussian contributions to the measurement errors. The λ test is insensitive to the scale of the σ_i. It is, however, sensitive to correlations introduced in calibration procedures. The extent to which this is a practical problem in using the λ test is a function of detector design and calibration. In particular we expect the λ test to be most useful in devices where the effect of calibrations is randomized over the measurements on a trajectory (e.g. in small cell drift chambers, where the drift direction changes layer by layer), and to be less effective in devices where coherent effects dominate (e.g. in detectors employing a jet cell design).

Potential uses for the λ test in charged particle tracking involve selecting decays in flight and enabling high quality track samples (with reduced non-Gaussian tails on the track parameter resolutions due to trajectory deviations) to be selected. Given the ease with which it can be calculated, a test on λ might serve as a filter for selecting tracks on which more computationally intensive tests [21,29] will be performed. The correlations measured by the ρ_k parameters may find use in a broader range of applications.